Frontiers in Heat Pipes (FHP), 2, 013002 (2011)
DOI: 10.5098/fhp.v2.1.3002

Global Digital Central
ISSN: 2155-658X

Frontiers in Heat Pipes

Available at www.ThermalFluidsCentral.org

USES OF LIQUID-METAL AND WATER HEAT PIPES IN SPACE REACTOR POWER SYSTEMS

Mohamed S. El-Genk[a,b,*] Jean-Michel P. Tournier[a]

[a] *Institute for Space and Nuclear Power Studies, Chemical & Nuclear Engineering Dept., University of New Mexico, Albuquerque, NM 87131, USA*
[b] *Mechanical Engineering Dept., University of New Mexico, Albuquerque, NM 87131, USA*

ABSTRACT

Water and liquid-metal heat pipes are considered for redundant and passive cooling of nuclear reactors and redundant operation of light-weight heat rejection radiators of space reactor power systems. The systems operate continuously for many years independent of the Sun, are enabling of deep space exploration and could provide 10's of kilowatts of electrical power for lunar and Martian outposts. Space reactors typically operate at 900 K – 1400 K could be cooled using liquid-metal heat pipes with either sodium (900 –1100 K) or lithium (1100 K–1400 K) working fluids. The heat rejection temperatures dictate the working fluid of the radiator heat pipes; potassium for 600 – 800 K, rubidium for 500 – 700 K, and water for $\leq$ 500 K. These working fluids would be frozen prior to starting up the power systems in orbit or at destination. The startup of water and liquid-metal heat pipes from a frozen state is complex, involving a number of non-linear mass and heat transport processes that require implementing appropriate procedures, depending on the type of working fluid. This paper reviews operation and design constraints pertinent to the uses of water and liquid-metal heat pipes in space reactor systems, and the modeling capabilities of the startup from a frozen state. In addition to models validation, results of design optimization of liquid-metal and water heat pipes in a number of space reactor power systems are presented and discussed.

Keywords: *Heat Pipes; Startup from frozen state; Space applications; Nuclear reactor cooling; Heat rejection radiator.*

1. INTRODUCTION

Liquid-metal heat pipes are considered for thermal energy transport in many high temperature and high power density space and terrestrial power and energy systems. A number of space reactor power system concepts have been developed or proposed with liquid-metal heat pipes for the passive and redundant removal and transport of the fission power generated in the reactor to the energy conversion subsystem (Angelo and Buden, 1985; El-Genk, 1994 and 2008b; Ranken, 1982 and 1990; Determan and Hagelston, 1992;, Poston et al., 2002; Ring *et al*., 2003; These heat pipes have also been considered for transporting waste heat from the energy conversion subsystems, and redundant and enhanced performance of heat rejection radiators. Energy conversion options considered for uses in space reactor power systems include Free-Piston Stirling Engine, FPSE (e.g., Angelo and Buden, 1985; Moriarty and Determan, 1989; Schreiber, 2001; Thieme *et al*., 2002 and 2004; Schmitz *et al*., 1994 and 2005), Thermoelectric (e.g., Ranken, 1982; Moriarty and Determan, 1989; Josloff *et al*., 1994; Marriott and Fujita, 1994; Caillat *et al*., 2000; El-Genk and Saber, 2003 and 2005; El-Genk *et al.*, 2006; El-Genk and Tournier, 2006b, El-Genk, 2008), Closed Brayton Cycle (CBC) with rotating turbo-machines (e.g., Harty and Mason, 1993; Shepard *et al*., 1994; Barrett and Reid, 2004; Barrett and Johnson, 2005; Gallo and El-Genk, 2009; El-Genk *et al*. 2010; El-Genk, 1994 and 2008), Potassium Rankine cycle (Angelo and Buden, 1985; Yoder and Graves, 1985; Bevard and Yoder, 2003), Thermionic (e.g., El-Genk and Paramonov, 1999; Ranken, 1990; Gunther, 1990; Merrigan and Trujillo, 1992; Determan and Hagelston, 1992; Begg *et al*., 1992; Mills *et al*., 1994; El-Genk, 1994; Paramonov and El-Genk, 1997) and Alkali-Metal Thermal-to-Electric (AMTEC) Conversion (e.g., Ryan *et al*., 2000; El-Genk and Tournier, 2002a and 2004a, El-Genk, 2008).

In these power systems, liquid-metal and water heat pipes have also been proposed for the heat rejection radiator panels, depending on the heat rejection temperature (e.g., Ranken, 1982; Angelo and Buden, 1985; El-Genk, Buksa and Seo, 1988; Moriarty and Determan, 1989; Gunther, 1990; Trujillo *et al*., 1990; Rovang *et al*., 1991; Harty and Mason, 1993; Marriott and Fujita, 1994; Josloff *et al.*, 1994; Juhasz and Rovang, 1995; El-Genk and Tournier, 2004a and 2006a; Schmitz *et al*., 2005; Tournier and El-Genk, 2006).

Besides offering passive thermal power transport at high rates, the heat pipes provide redundancy without failures propagation and single-point failures. Additional advantages of using heat pipes in space reactor power systems include passive and continuous removal of decay heat from the reactor core after shutdown; self containment, low inventory of working fluid (typically < 40 g/m); light-weight; near isothermal operation and high power throughput, up to 16 and 30 kW/cm^2 using Na and Li heat pipes, for operating at up to 1200 K and 1600 K, respectively (Merrigan, 1985). In addition, heat pipes

* *Corresponding author. Regents' Professor and Director, Institute for Space and Nuclear Power Studies*, (505) 277 – 7962, *Email*: *mgenk@unm.edu*

provide design simplicity, modularity, and integration flexibility. The utilization of alkali-metal heat pipes in space reactor power systems, however, requires proper selections of the working fluid, wick design and wick and wall materials. Such selections are based on considerations of operating temperature, chemical compatibility, creep strength and performance through the system's operation life (≥ 7 years). Candidate working fluids would be frozen at the startup of the power system in orbit or at destination (melting points of 273 K, 336.4 K, 370.9 K and 453.7 K, for water, potassium, sodium, and lithium, respectively). This requires a thorough understanding of the processes involved and developing proper procedures for a safe and reliable startup from a frozen state (El-Genk and Tournier, 2002b, 2004b; Tournier and El-Genk, 1995, 1996 and 2003).

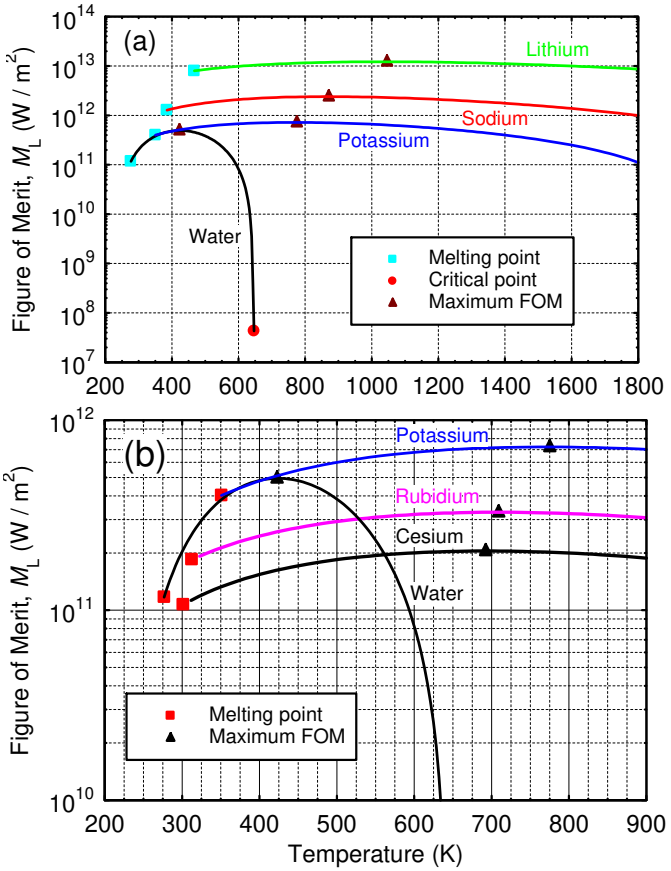

Fig. 1 Figure-Of-Merits (FOM) of heat pipe working fluids.

In space reactor power systems, it is generally desirable to operate alkali-metal heat pipes at a vapor pressure ≤ 0.1 MPa, or as close as practically possible to the temperature corresponding to the maximum Figure-of-Merit (FOM), M_L, of the working fluid (Figs. 1 and 2). Other selection criteria of alkali metal heat pipes for cooling nuclear reactors are low neutron activation of working fluid, and the possible generation of non-condensable gases by neutron capture. Heat pipes for uses in space reactor power systems are designed to operate nominally at 1/2 to 2/3 of the prevailing sonic and/or capillary limit.

Space nuclear reactors operating at 900 - 1400 K could be cooled using alkali-metal heat pipes with either sodium or lithium working fluid. The reactor exit temperature dictates the type of the heat pipes working fluid for cooling the reactor, and the heat rejection temperature dictates the type of the working fluid for the radiator's heat pipes. Suitable working fluids are water at 300 - 500 K, rubidium at 500 - 700 K, potassium at 600 - 800 K, sodium at 900 - 1100 K, and lithium at 1100 - 1400 K. These working fluids would be frozen prior to starting up the systems in orbit or at destination.

The startup of water and alkali-metal heat pipes from a frozen state is complex and involves a number of non-linear mass and heat transport processes. Examples are the enthalpy and momentum jump conditions at the solid-liquid and liquid-vapor interfaces, the progression in vapor transport from molecular, to transition and finally to continuum flow, and temperature-dependent transport and materials properties. Thus, thorough understanding of the various transport processes taking place is critical to developing appropriate startup procedures. These procedures strongly depend on the types of the working fluid and wick and the dimensions and design of the heat pipes. For example, though frozen alkali-metal heat pipes at a start up operate in the inefficient molecular flow regime up to elevated temperatures (Fig. 2a), a local dryout of the wick in the evaporator section is unlikely because of the increase in the specific volume of the working fluid upon melting. Conversely, while frozen water heat pipes start up in the efficient continuum flow regime (Fig. 2b), the input power during thawing should be kept sufficiently low to avoid causing a wick dryout because of the sublimation of the ice in the evaporator section and the decrease in the specific volume associated with melting of the ice.

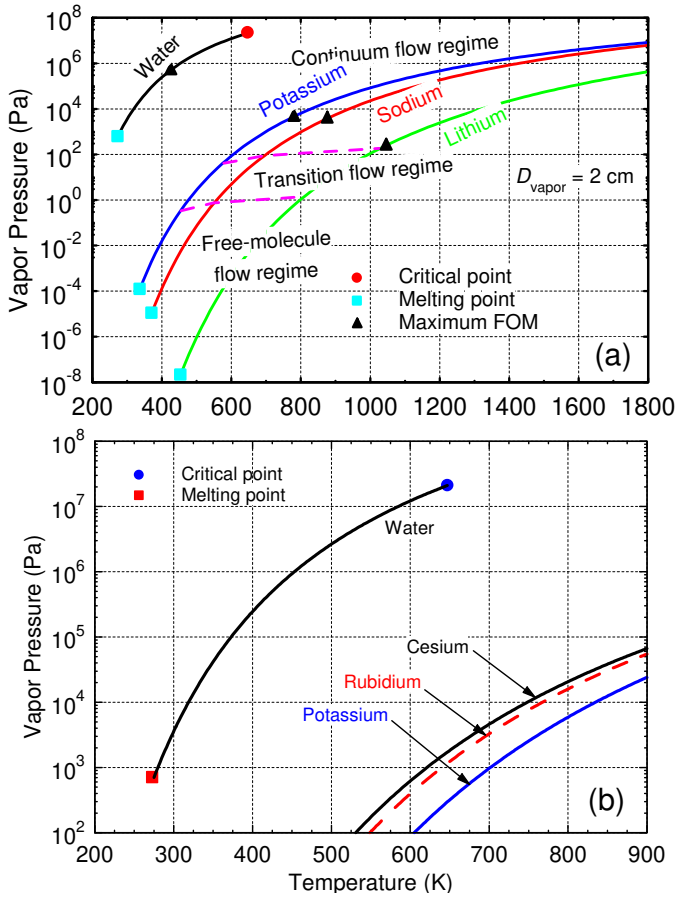

Fig. 2 Vapor pressure of heat pipe working fluids.

This paper reviews various operation and design constraints pertinent to using alkali-metal and water heat pipes for the passive and redundant cooling of the space reactors and operation of the waste heat rejection radiators. Also presented are the modeling capabilities and the results of models validation for the transient operation of alkali-metal and water heat pipes, including the startup from a frozen state. Results of the design optimization of heat pipes for reactor cooling and heat rejection radiator panels for a number of space power systems are also presented and discussed. The next section briefly reviews some of the fundamentals of heat pipes operation and design that are pertinent to the objectives of the paper.

Global Digital Central
ISSN: 2155-658X

2. FUNDAMENTALS OF HEAT PIPES

The ideal operation of a heat pipe is at the maximum of the FOM of the liquid working fluid, M_L, defined as (Fig. 1):

$$M_L = \sigma \rho_L h_{fg} / \mu_L \ . \quad (1)$$

In addition to the properties of the working fluid, the FOM bell shaped curves in Fig. 1 change significantly with temperature and extend from the melting to the critical point of the working fluid. At low temperature, the increase in FOM with temperature is dominated by decrease in liquid viscosity. Conversely, at higher temperatures, the decreases in both surface tension and latent heat of vaporization outweigh the decrease in liquid viscosity, causing the FOM to decrease with further increase in temperature (Fig. 1). Unlike the FOM curve for water, those of alkali-metals are quite flat, enabling a wide range of operating temperatures close to the maximum FOM (Fig. 1). Though viscosities of liquid Cesium (Cs) and Rubidium (Rb) are nearly identical, FOM for the latter is ~ 50% higher, because of its higher surface tension and volumetric latent heat of vaporization ($\rho_L h_{fg}$). The higher values of σ and ($\rho_L h_{fg}$) and lower viscosity of liquid potassium (K) increase its FOM to more than twice that of Rb.

For temperatures in the range 360 – 420 K, the FOM of water is comparable to that of potassium, but beyond 420 K, it drops precipitously due to decreasing surface tension and latent heat of vaporization (Fig. 1). At 500 K, the water vapor pressure is ~2.6 MPa (Fig. 2), requiring a thick wall, which increases the heat pipe mass and the temperature drop in the wall. Ideally, it is desirable to keep the vapor pressure in heat pipes $\leq$ 0.1 MPa. However, due to the absence of an alternative working fluid with a lower vapor pressure than water at temperatures > 400 K, radiator water heat pipes are designed to operate at up to 2.6 MPa and 500 K. Owing to the low rejection temperatures, CBC and FPSE energy conversions employ water heat pipes radiators (e.g., El-Genk and Tournier, 2006a).

Potassium (K), sodium (Na), and lithium (Li) working fluids span a wide range of operating temperatures from ~700 K to 1600 K. The saturation vapor pressures of water and K, Na and Li are compared in Fig. 2a. To ensure subsonic condition during operation, the nominal vapor pressure in alkali metal heat pipes is kept between 10 and 100 kPa, but becomes much lower at startup from a frozen state. In such a startup, the inefficient molecular vapor flow transports heat from the evaporator to the condenser and prevails up to high temperatures. This prolongs the startup to many hours (Deverall *et al*., 1970; Tournier and El-Genk, 1996; El-Genk and Tournier, 2002b).

To speed up the startup of alkali metal heat pipes from a frozen state, they may be loaded with a small amount of non-condensable or inert gas (Ponnappan *et al*., 1990). The added gas increases the total pressure in the heat pipe at start up, shortening the transition from the inefficient molecular and transition vapor flow regimes to the efficient continuum or viscous flow regime (Fig. 2). At the completion of startup to nominal steady-state power throughput, the added gas accumulates at the end of the condenser section, oversized for that purpose. On the other hand, when alkali-metal heat pipes are used in a neutron environment, such as in or near a nuclear reactor, gases may be generated by neutron capture in the alkali-metals. Unless accounted for in the design, these gases accumulate at the end of the condenser over time, gradually reducing its effective length for heat rejection, and hence the power throughput of the heat pipe.

For a 20 mm vapor core diameter, the operation of a Li heat pipe remains in the free-molecule flow regime up to 800 K (or vapor pressure < 1.4 Pa), the transition flow regime between 800 K and 1025 K, and the viscous regime above 1025 K (> 185 Pa) (Fig. 2a). For these regimes, the transition temperatures are 550 K (0.74 Pa) and 700 K (89 Pa) for sodium and 460 K (0.34 Pa) and 580 K (41 Pa) for potassium working fluids. During a startup of alkali-metal heat pipes from a frozen state, all three vapor flow regimes may co-exist along the heat pipe, depending on the location of the thaw front in the wick, and rates of heat input and removal in the evaporator and condenser sections, respectively.

In a successful startup from a frozen state the heat rejection from the condenser section remains nil until the heat pipe is fully thawed (Deverall *et al*., 1970). The sonic, capillary and entrainment limits could be successfully avoided by design; using large heat pipe diameter and/or small increases in heating rate. In addition to loading alkali-metal heat pipes with a small amount of non-condensable gases (Ponnappan *et al*., 1990; Faghri, 1995), speeding up the transition from the free-molecule to the continuum vapor flow regime could also benefit from increasing the length of the condenser section.

When alkali-metal heat pipes are used in the heat rejection radiator of a power system in which the reactor is also cooled by alkali-metal heat pipes, covering the radiator panels with an insulation blanket during startup and until heat pipes are fully thawed is recommended. After operating the reactor for months or years, the decay heat in the reactor core after shutdown would prevent the working fluid in the reactor's heat pipes from freezing for extended periods. In order to prolong the shutdown time of a nuclear reactor without freezing, the diameter of the radiator heat pipes could be made small to induce the sonic limit shortly after reactor shutdown (El-Genk, Buksa and Seo, 1988; El-Genk and Tournier, 2004a and 2006b). The resulting decrease in heat rejection would increase the time before the reactor working fluid freezes.

A reliable operation of heat pipes also depends on the selection of the materials for the wick and walls. Choices of wick and wall materials for high temperature heat pipes are presented next.

2.1 Structural Materials for Heat Pipes

The materials selection for the wick and wall of alkali-metal heat pipes depends on the operating temperature and pressure, type of working fluid, and operation environment, such as neutron irradiation in a nuclear reactor, mode of operation (e.g., steady or variable) and the operation life of the reactor power system (> 5 yrs). The choices of these materials, in order of increasing temperature, are titanium (Ta) and titanium (Ti) alloys, stainless steel, super-steel alloys, refractory metals (Nb, Mo, Ta and W) and refractory alloys (Nb-1Zr, PWC-11, TZM, T-111, Astar-811C, Mo-Re, W-Re) (Table 1). The service temperature of these materials depends on considerations of high-temperature creep strength; fabricability; effects of neutron irradiation on mechanical properties; chemical compatibility with heat pipe working fluid and nuclear fuel (UO_2, UC, or UN), when relevant; static and dynamic tensile behavior; fracture toughness; weldability and the ductile-to-brittle transition temperature (DBTT) (DiStefano, 1989; Zinkle *et al*., 2002; Buckman, 2004). For example, molybdenum (Mo) and tungsten (W) are brittle below ~ 400 K and 600 K, but alloying with rhenium (Re) decreases their DBTTs.

When operating in a fast neutron environment, such as in space nuclear reactor, the DBTTs of refractory materials and alloys increase significantly to $\geq$ 1000 K (El-Genk and Tournier, 2005). While operating at high temperatures partially decreases the material hardening due to neutron exposure, it also promotes grain growth that could weaken the wall strength and cause a leakage of the alkali-metal working fluid along the grain boundaries. A typical service temperature of heat pipes is the lowest of that corresponding to a vapor pressure < 0.1 MPa or to 40 – 60% of the melting temperature of the wall material, with a few exceptions such as the water heat pipes in the radiator panels of a space nuclear reactor power system with CBC or FPSE energy conversion.

Without an excessive over pressure, a failure of an alkali metal heat pipe could also be caused by the dissolution of the wall and wick materials in the evaporator section in the working fluid, and their transport and deposition in the condenser section. Other potential corrosion mechanisms of refractory metals and alloys by alkali metals are the chemical reactions with impurities, particularly non-metallic, such as oxygen, carbon, nitrogen and silicon (Reid *et al*., 1991; King and El-Genk, 2001). Corrosion failures could also result

Global Digital Central
ISSN: 2155-658X

Table 1 Selection of structural materials for heat pipes.

Material	Temp. (K)	Compatibility	Material	Composition (Elements > 1%)	Melting (K)	Density (g/cm^3)
Titanium	775 – 875	K	Titanium	Ti	1941	4.51
Steel alloys	875 – 900	Na, K, Hg	SS-304	Fe-19Cr-(8-12)Ni-2Mn	1699	7.92
			SS-316	Fe-17Cr-(10-14)Ni-2Mn	1658	7.9
Superalloys	900 – 1150	Na, K	Inconel 750X	73Ni-15.5Cr-7Fe-2.5Ti-1Nb	1666	8.25
		Na, K, NaK	Hastelloy X	49Ni-22Cr-15.8Fe-9Mo	1523	8.2
		Na	Haynes-25	50Co-20Cr-15W-10Ni-3Fe-1.5Mn	1602	-
Niobium alloys	Up to 1500	Li, Na, K	Niobium	Nb	2750	8.57
		Li, Na, K, NaK	Nb-1%Zr	Nb-1Zr	2680	8.58
			PWC-11	Nb-1Zr-0.1C	2680	8.60
			C-103	Nb-10Hf-1Ti-0.5Zr	2623	8.86
Molybdenum alloys	Up to 1800	Li, Na	Molybdenum	Mo (brittle below ~ 400 K)	2896	10.28
		Li, Na, K	Mo-TZM	Mo-0.5Ti-0.1Zr	2896	10.16
		Li	Mo-44.5%Re	Mo-44.5Re	3023	13.5
Tantalum alloys	Up to 2200	Li, Na, K, NaK, Hg, Cs	Tantalum	Ta	3290	16.6
			T-111	Ta-8W-2Hf	3250	16.7
			Astar 811C	Ta-8W-1Re-0.7Hf-0.025C	-	-
Tungsten alloys	Up to 2200	Li	Tungsten	W (brittle below ~ 600 K)	3695	19.25
			W-4%Re	W-4Re	-	18.35
Carbon	Up to 3000	Needs metal liner	Carbon	C	3923	2.25

Table 2 Operation life tests of alkali-metal heat pipes (Merrigan, 1985; Angelo and Buden, 1985; Houts *et al*., 1998; Rosenfeld *et al.*, 2004).

Fluid	Material	T (K)	Time (hrs)	Failure
Li	W-26Re	1875	10,000	
Li	TZM	1775	10,500	Weld cracking
Li	Nb-1Zr	1775	9,000	
Li	Mo-13%Re	1500	11,400	
Li	molybdenum	1700	25,400	Large grain formation, Li impurities
Na	Mo-TZM	1390	53,000	
Na	molybdenum	1400	45,000	
Na	300-series SS	970	115,000	
Na	Inconel-718	970	41,000	
Na	Haynes-230	970	20,000	
K	Nb-1%Zr	1350	10,000	
K	300-series SS	920	5,300	
K	titanium	800	5,000	
Hg	300-series SS	600	10,000	

from the reaction of trace amounts of impurities in the working fluid with the heat pipe wall and wick materials to form mobile compounds.

Many of these corrosion mechanisms could effectively be suppressed by proper selections of structural material and the working fluid (Table 1), by ensuring high-purity of the alkali metal working fluids, and using appropriate cleaning and filling procedures.

The results of life tests conducted at Los Alamos National Laboratory (Ranken, 1982; Merrigan, 1985; Merrigan and Trujillo, 1992; Reid *et al*., 1991) demonstrated good compatibility of various alkali metals with refractory metals and alloys (Table 2), provided that oxygen content is kept very low, less than 1–10 ppm (Reid *et al*., 1991; King and El-Genk, 2001). Niobium and tantalum are particularly susceptible to oxygen attacks in Na containing < 1-10 ppm O_2. Using refractory alloys containing traces of oxygen getters, such as Zr or Hf, helps alleviate this concern (DiStefano, 1989; King and El-Genk, 2001; El-Genk and Tournier, 2005); e.g. the niobium alloys Nb-1%Zr, PWC-11 and C-103 (Table 1).

Pure molybdenum and tungsten do not appear to be susceptible to oxygen-assisted alkali metal attack, as tantalum and niobium, but suffer from high DBTTs. This concern could be addressed by alloying these materials with other refractory metals. Examples are the molybdenum alloys TZM and Mo-Re (Table 1), which offer improved strength and ductility over pure Mo. Mo-13Re has excellent high-temperature creep strength, low-temperature ductility for launch conditions and excellent compatibility with lithium (> 11,000 hrs testing at 1500 K). Similarly, TZM and Na have excellent compatibility, tested for 53,000 hrs at 1390 K, without failures (Table 2).

2.2 Life and Irradiation Tests of Alkali Metal Heat Pipes

Life tests have been conducted of alkali-metal heat pipes with different working fluids and wall materials (Table 2). One of the longest life test to date is of a short lithium heat pipe fabricated from low-carbon, arc-cast Mo. It has operated successfully for 25,400 hrs continuously at 1700 K to transport ~ 1 kW (Ranken, 1982). This heat pipe experienced extensive grain growth in the wall, to the point that the grain size was several times the 1.0 mm thick wall. The lithium working fluid leaked out when this heat pipe was fastened onto a lathe to re-machine the support system (Ranken, 1982). Other issues that may affect the operation life and degrade the performance of alkali metal heat pipes are changes in the surface tension and wetting characteristics of the working fluid due to the presence of small amounts of impurities, and in the wick hydraulic characteristics, including reduced permeability and/or increased average pore sizes.

The use of alkali metal heat pipes for cooling space nuclear reactors has been demonstrated in a number of prototype experiments. A total of 29 heat pipes have been operated in high, fast neutron fluence with no reported failures (Determan and Hagelston, 1992; Houts *et al*., 1998). Nineteen SS/Na heat pipes and eight SS/K heat pipes have been tested in the Experimental Breeder Reactor (EBR-II), both in gravity-assisted and gravity–opposed positions, without failures. Individual testing periods of these heat pipes in the EBR-II core varied from 1,100 to 23,000 hours, for a total cumulative testing time of 137,000 hours. The tested heat pipes operated at 900 – 1100 K and a power throughput of 0.5 to 5 kW in a fast neutron fluence of 0.27 – 10 x 10^{22} n/cm^2. These fluences are about an order of magnitude higher than that typically encountered in a space nuclear reactor operating continuously for 7 – 10 years.

Neutron activation of the alkali metal working fluid of tested heat pipes generated non-condensable gases, which accumulated at the end of the condenser section, gradually decreasing the heat rejection capability and the power throughout over time. For example, ^{6}Li, with an abundance of 7.4 at% and 1.0 at% in natural and depleted lithium, respectively, absorbs neutrons to produce tritium and helium gases. The cross-sections for these reactions are 945 barns for thermal neutrons (< 0.1 eV) and 0.12 barn for fast 100-keV neutrons. Also, the naturally occurring potassium isotope ^{39}K absorbs thermal neutrons with a cross-section of 1.94 barns to produce hydrogen and argon gases.

Global Digital Central
ISSN: 2155-658X

2.3 Operation Limits of Heat Pipes

Alkali metal heat pipes can operate near the maximum FOM over a broad range of temperatures, depending on the type of working fluid (Fig. 1). The operation limits of a heat pipe (Fig. 3), in the order of increasing power throughput and temperature, are the viscous, sonic, wicking or capillary, entrainment, boiling, and heat rejection. The latter is dictated by the length of the condenser section, surface emissivity and available area for heat rejection in the radiators for space nuclear reactor power systems.

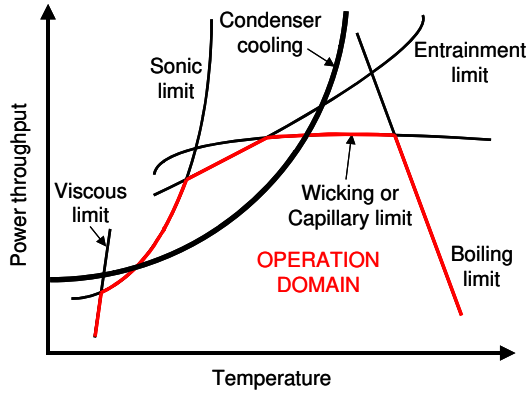

Fig. 3 Operation limits of a heat pipe.

The viscous limit dominates at low temperature, near the melting point of the working fluid. The high liquid pressure losses in the wick, due to the high viscosity and low permeability, limit liquid flow from the condenser to the evaporator section. Avoiding this limit requires operating at a relatively low input power until the heat pipe temperature is high enough to decrease the liquid viscosity and hence, the pressure losses in the wick.

The sonic limit, also dominant at low temperatures, should be avoided. The vapor pressure of the working fluid is a good indicator of reaching this limit (Fig. 2). Below ~ 1 kPa, the vapor flow in alkali-metal heat pipes is not continuum, but rather molecular or transition, meaning that the power transport capabilities are limited due to the very low vapor density, which also results in a high Mach number. The nominal operation vapor pressures of the potassium, rubidium, and cesium heat pipe working fluids are > 1 kPa above 700 K, 640 K and 620 K, respectively. Below these temperatures, avoiding the sonic limit requires using large diameter heat pipes. While liquid cesium and rubidium could be used in heat pipes at lower temperatures than potassium (Fig. 2), the latter provides significantly higher performance at ~750 K (Fig. 1).

Because water has much higher vapor pressure, the sonic limit is not a concern in water heat pipes. Unlike alkali-metals, the flow of water vapor in heat pipes is always in the continuum regime, even during the startup from a frozen state. However, for practical considerations, the operation of water heat pipes is limited to $\leq$ 500 K. Thus, water heat pipes may be used in the heat rejection radiator panels of space reactor power systems with average radiator temperature from 350 to 500 K. On the other hand, alkali metal heat pipes (with Cs, Rb or K working fluids) could be used in radiators operating at 650 – 800 K. It has long been a challenge to find a suitable heat pipes working fluid for the temperature range ~ 450 – 700 K; however, some promising ones, such as iodine and antimony tri-bromide, have been investigated (Anderson, 2005).

The capillary (or wicking) limit is encountered when the net capillary pressure head is less than the combined pressure losses of the liquid flow in the wick and of the counter-current vapor flow in the heat pipe (Eq. 2). The capillary pressure head for circulating the heat pipes working fluid increases with increasing the liquid surface tension and decreasing radius of curvature of the liquid-vapor meniscus in the surface pores in the wick, R_c (Fig. 4). The maximum theoretical capillary pressure head attainable is when R_c equals the effective pore radius in the wick, R_p. Thus, in space applications in order to avoid encountering the capillary limit, the following condition needs to be satisfied:

$$(\Delta P_{cap}^{ev})^{\max} = \frac{2\sigma(T_{ev})}{R_p} \geq \Delta P_{cap}^{cd} + \Delta P_L + \Delta P_V \,. \tag{2}$$

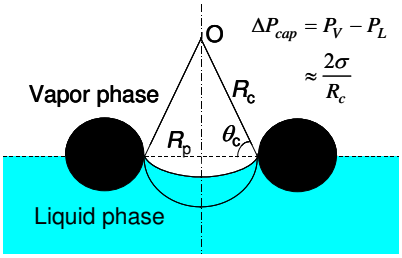

Fig. 4 Capillary pumping of the working fluid in a heat pipe.

The total liquid pressure losses in the wick along the heat pipe are:

$$\Delta P_L = \frac{1}{KA_w}\int_0^L \nu_L \dot{m}(z)\,dz = \frac{\dot{m}\bar{L}}{KA_w}\bar{\nu}_L = \frac{\bar{L}Q}{KA_w}\frac{\bar{\nu}_L}{h_{fg}(T_{ev})} \,. \tag{3}$$

The pressure drop in the vapor region, ΔP_V, is practically negligible ($\Delta P_V << \Delta P_L$). Furthermore, the pores of the wick near the end of the condenser section would be flooded by the accumulation of excess liquid (i.e, $\Delta P_{cap}^{cd} = 0$). Thus, the heat pipe capillary limit can be expressed as:

$$Q_{cap}^{\text{limit}} \cong \left(\frac{2KA_w}{R_p\bar{L}}\right)\times\left(\frac{\sigma(T_{ev})h_{fg}(T_{ev})}{\bar{\nu}_L}\right) = \left(\frac{2KA_w}{R_p\bar{L}}\right)\times M_L \,. \tag{4}$$

The first term on the right hand side of Eq. (4) is a function of geometry and effective permeability of the wick, and M_L is a function of the physical properties of working fluid (Fig. 1). The capillary limit can be raised either by increasing the capillary pressure head and/or decreasing the liquid pressure losses in the wick. The former is achieved by decreasing the effective pore size in the wick, while the latter would be possible using longitudinal grooves on the inside of the heat pipe wall, an annular wick geometry with a small (~ 0.4 mm) liquid gap between the wall and the wick, or liquid arteries (e.g., Ivanovskii *et al.*, 1982; Merrigan, 1985; Reid *et al.*, 1999; Glass *et al.*, 1999, Faghri, 1995; Reay, 2006). While arteries may increase the design complexity and fabrication cost, they significantly increase the power throughput. The commonly used homogeneous wicks, made of a wrapped wire–screened mesh or a ceramic or metallic powder are relatively simple and could be quite effective, but may increase the liquid pressure losses.

The entrainment limit is typically encountered during a heat pipe startup, when the vapor flow at the evaporator section exit is chocked (velocity is near sonic). The induced interfacial shear stress at the surface of the liquid saturated wick, by the vapor counter-current flow could not only slow down the liquid flow to the evaporator section, but also break up and entrain tiny liquid droplets back to the condenser. The reduced replenishing of the wick in the evaporator section with liquid could result in a local dryout. The entrainment limit could be raised by employing a small pore size wick and/or increasing the cross-sectional flow area for the vapor in the heat pipe to lower its velocity at the exit of the evaporator section.

A boiling at the inside surface of the heat pipe wall in the evaporator section is likely when the local liquid superheat exceeds that for incipient nucleate boiling. The ensuing nucleation and growth of vapor bubbles blocks the flow of returning liquid to the evaporator section. In alkali-metal heat pipes, the boiling limit is typically encountered at high wall temperatures, beyond those selected for nominal operation.

An additional operation limit, often overlooked, is that of heat rejection in the condenser section. In space reactor power systems, the condenser section of the radiator heat pipes is cooled by thermal

Global Digital Central
ISSN: 2155-658X

radiation into outer space. Therefore, the heat removal rate is proportional to the effective surface emissivity and area in the condenser section and the average surface temperature to the fourth power. Metallic surfaces typically have low emissivity, thus are treated with a black coating or paint to improve heat rejection. This operation limit might be encountered late in life, due to the accumulation of non-condensable gases, generated by neutron activation, at the end of the condenser, gradually decreasing the rate of heat rejection.

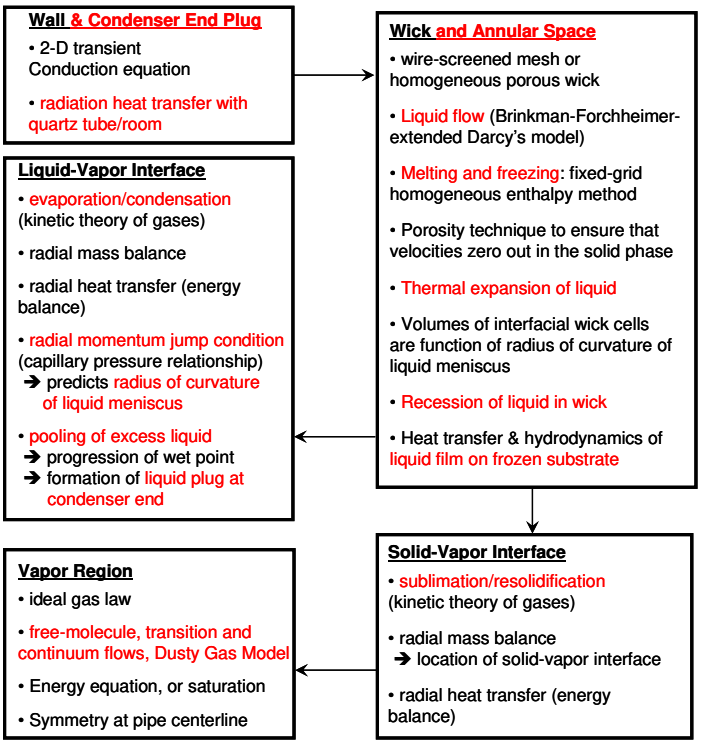

Fig. 5 A block-diagram of HPTAM capabilities and sub-models.

3. TRANSIENT MODELING OF HEAT PIPES

Reid *et al*. (1991) have published a comprehensive review of alkali-metal heat pipes research until 1991 and cover both modeling and experimental investigations of transient and steady state operation, including the startup of alkali and water heat pipes from a frozen state. The reported models by various investigators for simulating the startup of alkali metal heat pipes from a frozen state have recently also been reviewed (Tournier and El-Genk, 2002; El-Genk and Tournier, 2002b). The capabilities of the Heat Pipe Transient Analysis Model (HPTAM) have been demonstrated for the transient operation of low-temperature (e.g. water and ammonia) and high-temperature (e.g. rubidium, cesium, potassium, sodium, and lithium) heat pipes and for the simulation of the startup of water and alkali-metal heat pipes from a frozen state (Tournier and El-Genk, 1995, 1996, 2002, 2003, 2006; El-Genk and Tournier, 1995, 2002b, 2004b, 2006a,b; Huang and El-Genk, 1993).

3.1 Capabilities of HPTAM

The Heat Pipe Transient Analysis Model (HPTAM) is a 2-dimensional code for simulating the transient operation of heat pipes, including the startup from a frozen state. For the latter, it simultaneously accounts for the sublimation and resolidification processes at the wick surface (essential in the startup of low-temperature heat pipes from a frozen state) and incorporates detailed sub-models for the continuum and non-continuum vapor flow regimes (free-molecular and transition) using the Dusty-Gas-Model (El-Genk and Tournier, 1995; Tournier and El-Genk, 1996).

HPTAM tracks the thawing front of the working fluid in the wick using a numerically stable homogeneous enthalpy method. It thermally and hydro-dynamically couples the momentum, continuity and energy equations at the solid-vapor and liquid-vapor interfaces and determines the partial recession of the liquid in the wick and the pooling of excess liquid during startup transients. It solves the transient heat conduction equations in the wall and the condenser end plug, if any, and uses the Brinkman-Forchheimer-extended Darcy's equations to predict the liquid flow in the porous wick (Scheidegger, 1974; Tournier and El-Genk, 1995). It treats both the annular wire-screened mesh and homogeneous porous wicks. The various sub-models and features in HPTAM are outlined in Fig. 5.

For simulating the startup of an alkali-metal heat pipe from a frozen state, the numerical solution is stable and faster than real time and the modeling capabilities in HPTAM include the following: (a) the radial and axial propagation of the thaw front in the wick; (b) the free-molecule, transition and continuum flow regimes in the vapor core, and their transient propagation towards the end of the condenser; (c) the volume expansion of working fluid upon melting and heating above melting point; (d) the liquid evaporation and resolidification onto the frozen wick of the heat pipe downstream, the condensation of vapor and the entrainment of liquid by the vapor flow; (e) the accumulation of excess liquid and non-condensable gases, if any, at the end of the condenser section; and (f) liquid recession and the potential for a dryout in the evaporator wick.

3.2 Validation of HPTAM for Startup from a Frozen State

The predictions of HPTAM have been successfully validated with experimental results for water and alkali metal heat pipes (Reid, 1999; Tournier and El-Genk, 1995, 1996, 2002, 2003, 2006; El-Genk and Tournier, 1995, 2002b, 2004b, 2006a,b; Huang *et al*. 1993). The freeze-and-thaw capabilities in HPTAM have been successfully validated using one-dimensional exact solutions for a pure conduction phase-change (Ozisik, 1980), and the analytical solution for the two-dimensional problem of freezing in a corner (Rathjen and Jiji, 1971). The experimental data of Wolff and Viskanta (1988) have also been used to benchmark the freeze-and-thaw capabilities in HPTAM.

The Dusty Gas Model in HPTAM, for simulating the non-continuum vapor flow regimes, has also been validated (El-Genk and Tournier, 1995) using the experimental data of Knudsen (Loeb, 1934), of carbon dioxide gas flow at room temperature through a bundle of 24 capillary tubes (2 cm-long, 67 μm in diameter). HPTAM's predictions successfully compared to the reported experimental data for the startup of a radiatively-cooled, SS-304L/sodium heat pipe from a frozen state (Faghri *et al*., 1991). The calculated wall temperatures during the startup transient were in good agreement with those measured (Tournier and El-Genk, 1996 and 2002).

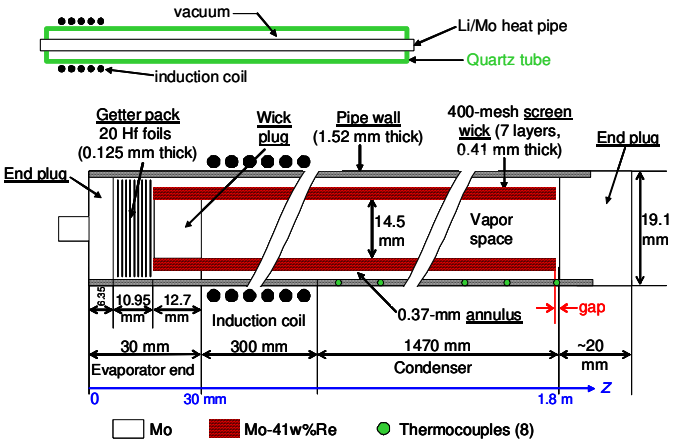

Fig. 6 Cutaway views of Mo-Li heat pipe (Reid *et al*., 1999).

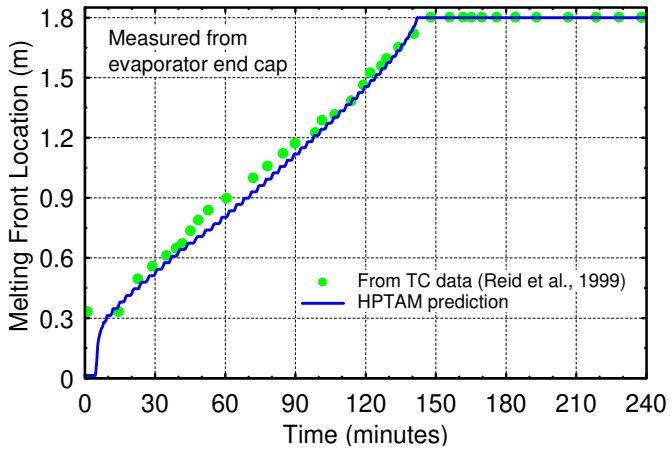

Fig. 7 Melting front location in Mo-Li heat pipe during startup.

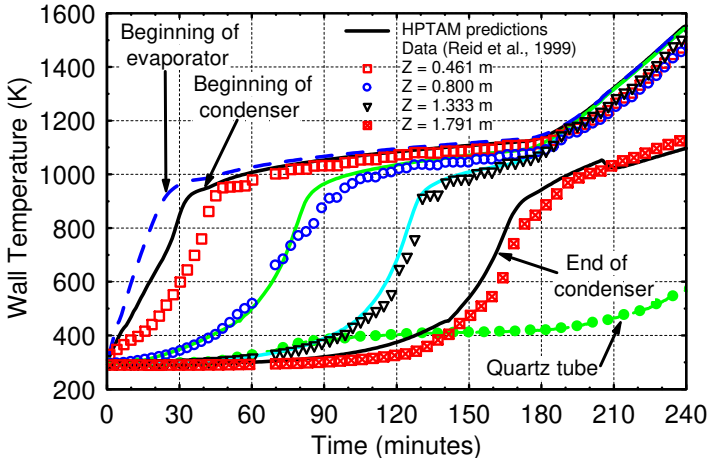

Fig. 8 Wall temperatures during Mo-Li heat pipe startup.

HPTAM has also been used to simulate the startup of a Mo/Li heat pipe from a frozen state and its predictions have been favorably compared with the reported results of tests performed at LANL (Reid *et al*., 1999; Tournier and El-Genk, 2003). The tested heat pipe was 1.8 m-long and had a Mo-41%Re wick made of 7 layers of a 400-mesh screen (Fig. 6). The screen wick was 0.41 mm thick, and had an effective pore radius of 19.3 μm, calculated volume porosity of 0.7093 and permeability of 2.167 x 10^{-11} m^2. The 30 cm-long evaporator section was inductively heated, and the 147 cm-long condenser was cooled by thermal radiation to an evacuated quartz tube surrounding the heat pipe (Fig. 6).

Modeling the startup of this heat pipe in the experiment required incorporating new capabilities in HPTAM. These are modeling the mass, momentum, and heat transfer in the annular space between the porous wick and the heat pipe wall; simulating the radiation heat exchange between the pipe wall and both the semi-transparent quartz tube and ambient, using a two-waveband approximation; and adding capabilities for predicting the accumulation of excess liquid at the end of the condenser (Tournier and El-Genk, 2003). Also, a procedure was developed to estimate the net thermal power input to the inductively-heated evaporator section of the heat pipe in the test, based on the measured wall temperature and after accounting for the radiation heat losses along the condenser section. The rate of thermal energy storage in the solid structures of the heat pipe and the working fluid before reaching steady state was also accounted for in HPTAM (Tournier and El-Genk, 2003).

In the numerical simulation of the startup of the Li/Mo heat pipe from a frozen state, the evaporator section was discretized into 9 axial computational cells, and the condenser section into 44 axial cells. In the radial direction, 4 computational cells were used in the pipe wall. The simulation of the four-hour startup transient used a variable time step of 125 – 250 ms. At steady state, the heat pipe transported 4.0 kW. The corresponding power throughput and the net evaporator radial heat flux were 2.4 kW/cm^2 and 22.2 W/cm^2, respectively.

The Mo-Li heat pipe in the test started successfully, without a dryout of the wick or the liquid annulus in the evaporator section. The predictions of the melting front location (Fig. 7) and of the wall temperature along the heat pipe (Figs. 8 and 9), at different times during the startup in the horizontal position, were in good agreement with measurements (Reid *et al.*, 1999). When the heat pipe reached steady-state at an evaporator temperature of 1550 K, the wall temperature near the end of the condenser dropped precipitously by 450 K (Figs. 8 and 9). Such a drop is due to a 8.3 cm-long pool of excess liquid and heat losses from the condenser end plug. The extent of the liquid pool was estimated, based on the temperature measurements and visual observations, to be ~ 9 cm (Reid *et al*., 1999), which is in good agreement with predictions (Fig. 9).

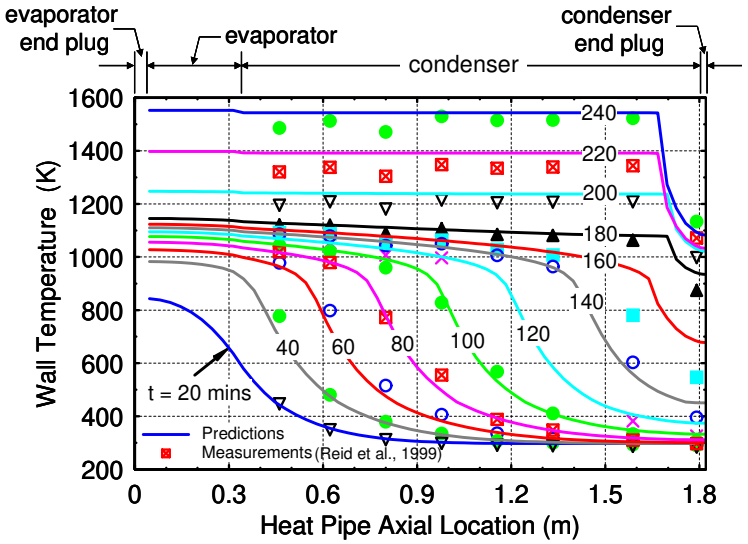

Fig. 9 Axial temperatures during Mo-Li heat pipe startup.

3.3 Validation for Steady-State Operation

A simplified version of HPTAM has also been developed to perform analyses and optimize the design of heat pipe radiator panels for space reactor power systems (UNM-HP). This one-dimensional steady-state model calculates the vapor pressure losses in the various zones of the heat pipes (evaporator, adiabatic, and condenser), when the flow is dominated by friction rather than inertia forces (vapor Mach number < 0.5). To account for the vapor compressibility, the local vapor density is expressed as a function of pressure and temperature using the perfect gas law. The estimated vapor pressure loss is used to calculate the temperature drop in the vapor along the heat pipe.

This temperature drop is added to those in the wall, liquid annulus, and wick structure, both in the condenser and evaporator sections, to determine the total temperature drop along the heat pipe. This one-dimensional model is applicable to cesium, rubidium, potassium, sodium, and lithium working fluids and incorporates a number of wick structures and wall materials. It calculates various operation limits; namely, viscous, sonic, capillary, entrainment, and incipient boiling for the design of reactor and radiator heat pipes (El-Genk and Tournier 2004a,b, 244b, 2006a; Tournier and El-Genk, 2002, 2004, 2006).
UNM-HP has also been validated with steady-state data for a near-horizontal sodium heat pipe with a 10 cm long evaporator, 5 cm long adiabatic section, and a variable condenser length (Ivanovskii *et al*., 1982). The vapor core diameter is 1.4 cm, and the 70 cm-long heat pipe has an annular wick with a 0.5 mm liquid gap under a porous shield. The vapor temperature along the heat pipe was measured using a movable micro-thermocouple. Such measurements are rare and, to the

best of the authors' knowledge, none have been reported for longer liquid metal heat pipes, but similar measurements have been reported for water heat pipes (El-Genk *et al*., 1995; Huang and El-Genk, 1993).

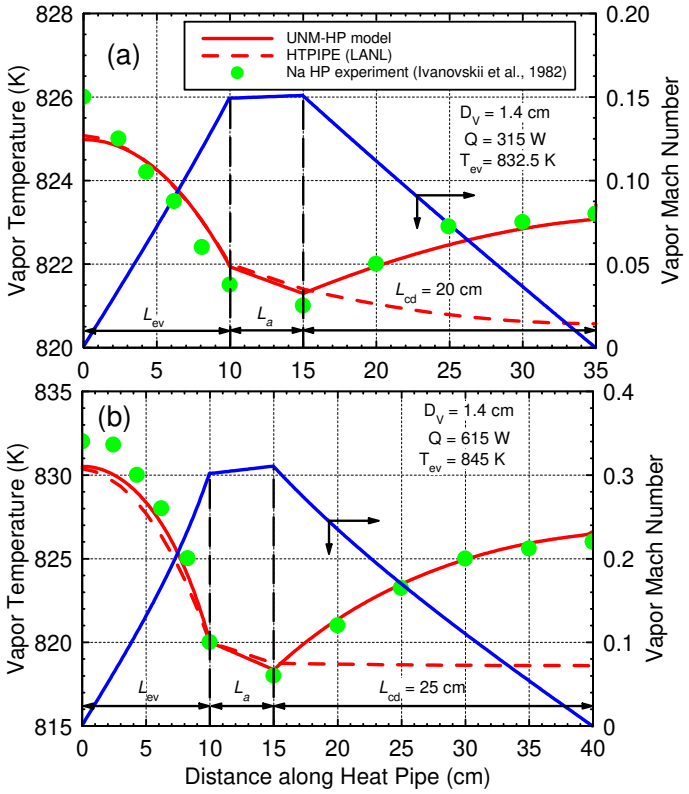

Fig. 10 Comparison of UNM-HP predictions with experimental data for a Na heat pipe (data from Ivanovskii *et al*., 1982).

The results in Figs. 10a and 10b indicate that at power throughputs of 315 W and 615 W, the vapor Mach number at the evaporator exit is 0.15 and 0.3. The vapor pressure and temperature fall rapidly along the short evaporator length due to friction and inertia pressure losses. The later are nil in the adiabatic section, where the vapor pressure decreases linearly with distance due to friction losses. As shown in Figures 10a and 10b, the inertia pressure gain dominates, leading to a net pressure recovery along the condenser length.

The predictions of UNM-HP are in excellent agreement with the experimental data for the vapor temperature along the heat pipe (Figs. 10a and 10b). The predictions by the widely used HTPIPE model (Prenger, 1979; Woloshun *et al*., 1989) are also shown in Figs. 10a and 10b. HTPIPE, developed at LANL (Woloshun *et al*., 1989), is based on the methodology of Busse (1967) for laminar vapor flow. It did not predict the pressure recovery in the condenser, suggesting an under-prediction of the inertia effect. The predictions of HTPIPE are reasonable in the evaporator and adiabatic section, short of predicting the pressure recovery in the condenser section.

3.4 Validation of HPTAM for a Sodium Heat Pipe Startup

The successful comparison of HPTAM's predictions in Figs. 11 and 13 with the experimental results of Faghri *et al*. (1991) demonstrates the various processes taking place during the startup of the radiatively-cooled, SS-304L-sodium heat pipe from a frozen state (Tournier and El-Genk, 1996). The effective lengths of the evaporator, adiabatic and condenser sections of the heat pipe (Faghri *et al*. 1991) were 5.3 cm, 61.7 cm and 29.2 cm, respectively. The circumferential wick was made up of two wraps of 100-inch^{-1} mesh SS screen, having a wire diameter of 114 μm, effective pore radius of 70 μm, and a porosity of 0.70. The heat pipe, charged with 30 grams of Na, was tested in a vacuum chamber at an ambient temperature of 290 K. The measured surface emissivity of the condenser was 0.645. For the vapor core diameter of 21 mm, the transition temperatures to the continuum, transition and free-molecule flow regimes, corresponding to Knudsen numbers of 0.01 and 1 are 686 K and 540 K. Initially, the Na in the wick was frozen at a uniform temperature of 290 K (Faghri *et al*. 1991).

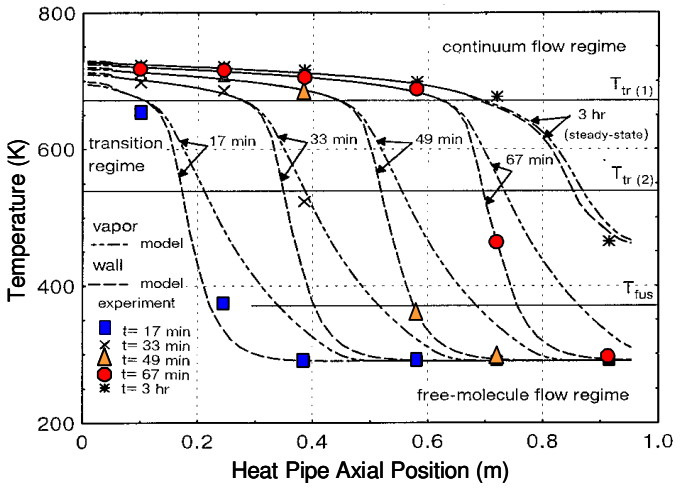

Fig. 11 Axial temperature distributions in Na heat pipe (data from Faghri *et al*., 1991).

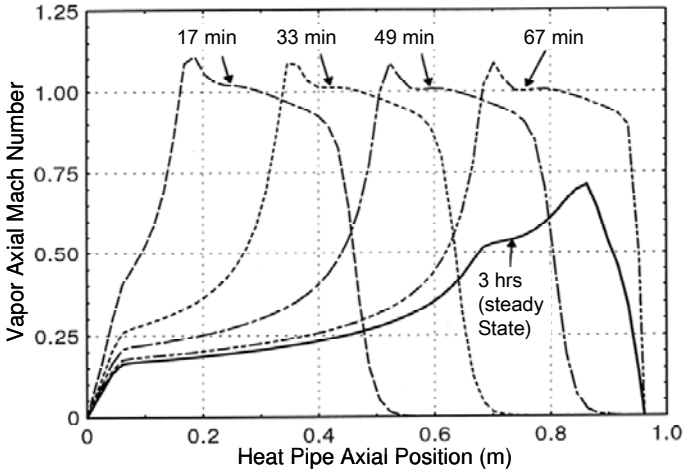

Fig. 12 Predicted vapor Mach number in Na heat pipe.

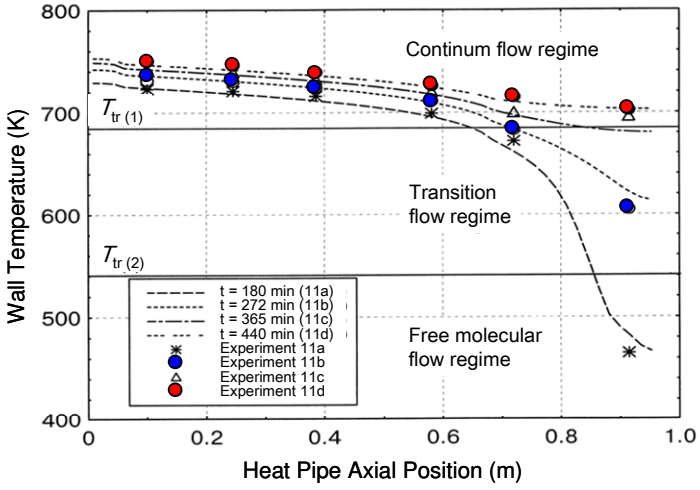

Fig. 13 Steady-state operation of Na heat pipe (Faghri *et al*., 1991).

Results in Figs. 11 and 13 show an excellent agreement of the model predictions with the measured wall temperature. Fig. 12 shows

Global Digital Central
ISSN: 2155-658X

the calculated vapor Mach number along the Na heat pipe at different times during the startup transient. The startup was initiated by increasing the input power to the evaporator section from zero to 119 W with an exponential period of 50 s. After ~ 2 minutes into the startup transient, the Na at the evaporator wall melted, and the melting front propagated radially inward (Fig. 14a).

Although sublimation of solid Na in the evaporator wick and solidification at the solid-vapor interface in the condenser occurred, the amount of Na transported was negligible, owing to the very low vapor pressure. Complete melting of the Na in the evaporator occurred very rapidly, in less than a minute, and evaporation of liquid Na occurred at the L-V interface. However, the vapor flow was still rarefied or in the molecular flow regime. As Na evaporation continued, the vapor accumulation increased its pressure, transitioning the vapor in the evaporator to the transition flow regime (Figs. 2a and 14b). After about 8 minutes into the startup transient, the continuum vapor flow was established along the evaporator section, at which time the vapor temperature reached roughly 686 K (Figs. 2a and 14c). The vapor flow choked at the evaporator exit, while in the remaining length of the heat pipe it was still in the molecular flow regime (Figs. 12 and 14c).

After the Na in the evaporator wick was fully thawed, the melting and the continuum vapor flow fronts propagated axially toward the condenser (Fig. 14d). It took these fronts about 50 additional minutes to traverse the 61.7 cm-long, adiabatic section at an average velocity of ~ 1.2 cm/min. During this period, most of the heat input was utilized in the vaporization of liquid Na in the evaporator section, and the heat pipe length could be divided into several sequential zones (Fig. 14d). In zone (I) of the evaporator, the Na vapor flow was in the continuum regime. The evaporation occurred uniformly along the L-V interface, increasing the vapor velocity linearly along the evaporator section. In zone (II) within the adiabatic section, the vapor flow was also in the continuum regime, with only minimal condensation occurring at the L-V interface. The vapor flow accelerates, however, due to the slow decreases in its temperature and density. In zone (III), also in the adiabatic section, the vapor pressure and temperature are lower and the vapor flow is in the transition regime (Fig. 2).

The continuum vapor flow front moved forward toward the condenser, where the condensation of vapor raised the wick and wall temperatures (Fig. 14d). In zone (IV), also in the adiabatic section, where the Na vapor flow was in the transition regime, the vapor velocity became slightly supersonic, over a short distance, at a Mach number between 1 and 1.1 (Fig. 12). Finally, in zone (V), solidification of Na vapor occurred at the solid-vapor interface in the wick, with still solid Na. However, only a minimal amount of Na was involved. The vapor axial flow velocity decreased steadily as the thaw front proceeded axially along the condenser section. Though the vapor velocity in zone IV was subsonic, it was still significant due to the very low vapor density (Fig. 12).

Once the continuum vapor flow front reached the condenser section, the condenser started radiating heat away (Fig. 14e), slowing the axial propagation of the thaw and the continuum vapor flow fronts. The heat pipe approached steady-state operation after the Na working fluid in the heat pipe was fully thawed, the vapor along the entire length of the heat pipe was in the continuum flow regime, and the rate of heat rejection in the condenser equated the input in the evaporator. At steady state, the Na condensation was uniform along the active length of the condenser section, and the vapor axial velocity became subsonic everywhere, with a maximum Mach number of 0.70 (Fig. 12). The excess liquid Na formed a liquid pool at the end of the condenser.

3.5 HPTAM Simulation of a Water Heat Pipe Startup

The simulated startup of a water heat pipe from a frozen state (Tournier and El-Genk, 1995) may be divided into several successive steps (Fig. 15a). Initially, the water in the wick is frozen and as thermal power is applied to the evaporator section the ice in the wick sublimes. The water vapor transports as a continuum flow to the condenser where it solidifies (Fig. 15b). This sublimation / solidification process depletes the ice in the evaporator's wick and accumulates it in the condenser (Fig. 15b). As the wall temperature in the evaporator continues to increase, the ice in the wick at the evaporator wall begins to melt (Fig. 15c).

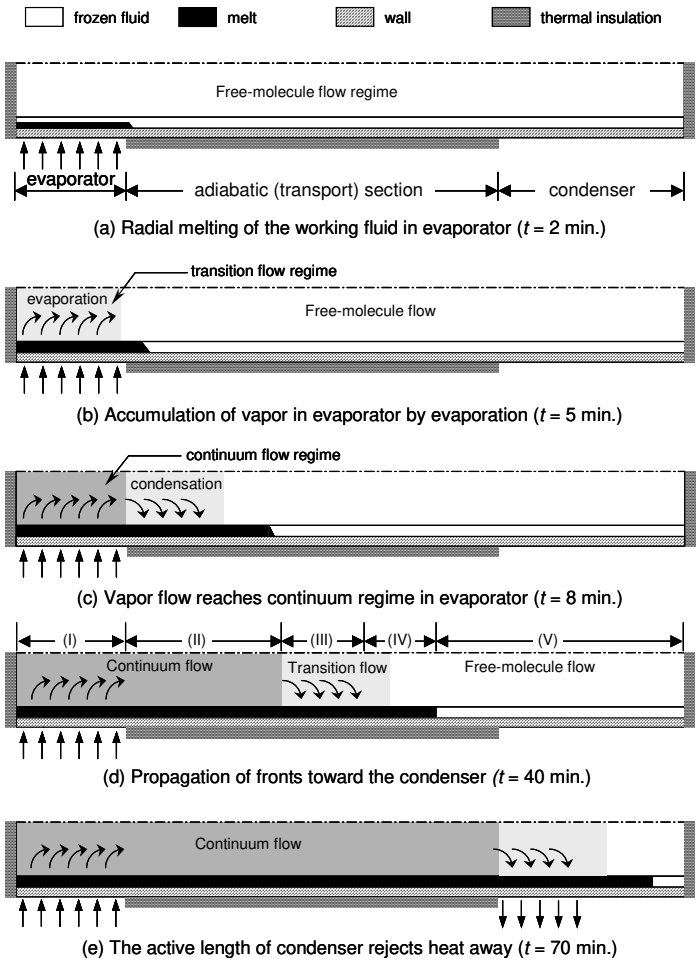

Fig. 14 Startup progression of a sodium heat pipe from a frozen state.

The thaw front progresses radially and axially, and when it reaches the liquid–vapor interface (Fig. 15d), the following takes place:

(a) Vaporization depletes water in the evaporator wick, particularly since the density increases upon melting. Such a decrease in density, unless the input power to the evaporator is kept very low, could cause a dryout in the wick.

(b) A thin liquid film of water condensate forms onto the ice substrate in the condenser. The drainage of the water film back to the evaporator, governed by the balance of the capillary effect and frictional drag at the film–ice interface, could prevent or postpone a dryout in the wick (Fig. 15d).

(c) In addition to the two-dimensional progression of the thaw front in the wick toward the condenser, melting may also occur in the condenser and adiabatic sections at the water film/ice interface and proceed radially outward.

(d) Eventually, the heat pipe becomes fully-thawed and the water circulation in the wick is established (Fig. 15e). Because of the relatively high pressure of water vapor, even near the ice melting point, choked and/or supersonic vapor flows are not encountered during the startup. However, the input power to the evaporator should be kept low enough to avoid boiling or dryout of the wick, particularly before the water film flow from the condenser to the evaporator is established.

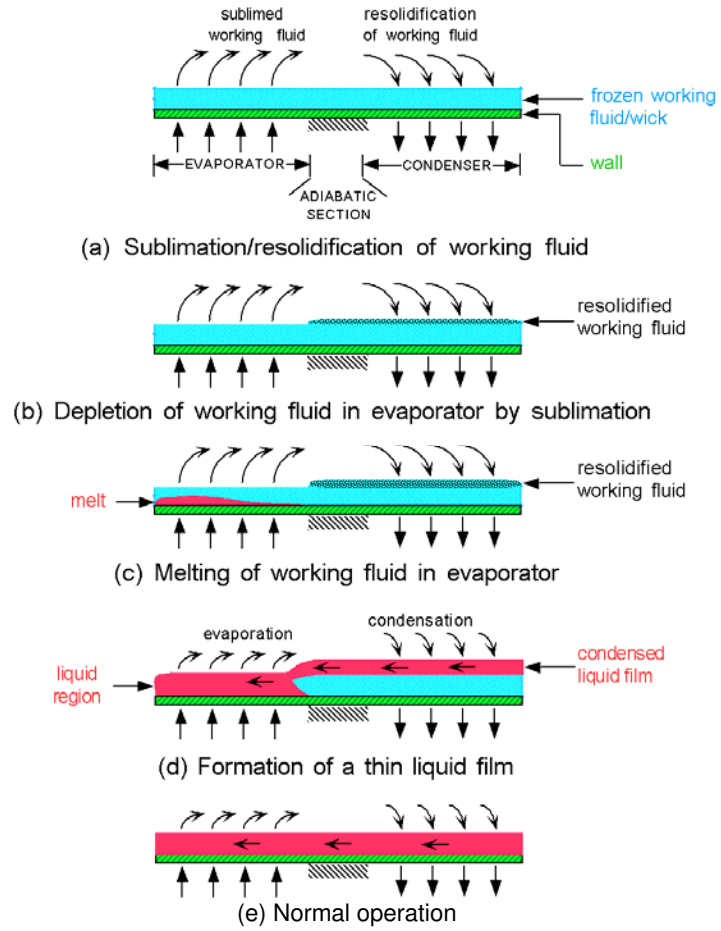

Fig. 15 Illustration of startup of water heat pipe from a frozen state.

4. RADIATOR HEAT PIPES DESIGN

Figure 16 shows a typical, fully deployed space nuclear reactor power system (El-Genk, 2008a,b; El-Genk and Tournier, 2006b) with a liquid-metal heat pipes radiator. The power systems also has six pairs of primary and secondary loops with circulating liquid-metal working fluids, and thermoelectric energy conversion elements thermally coupled to the primary and secondary loops. The liquid-metal heat pipes radiator has six panels, each consists of a forward fixed segment and 2 rear deployable segments for waste heat rejection (Figs. 17 and 18).

The stowed configuration and deployment sequence of the radiator panels is shown in Fig. 19. When the 12 rear segments of the radiator panels are folded onto the 6 forward segments, the stowed power

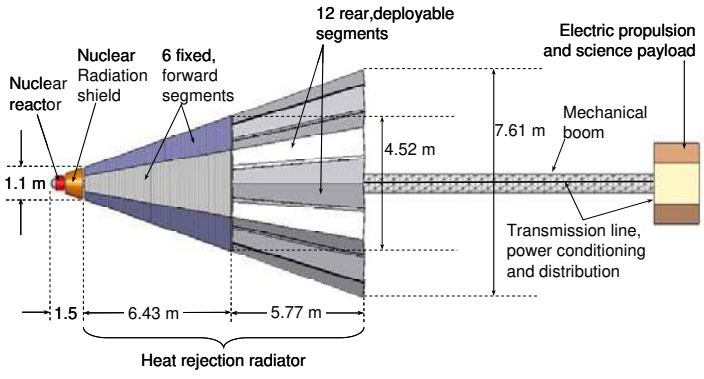

Fig. 16 A Space reactor power system with a fully deployed radiator (El-Genk, 2008a,b; El-Genk Tournier 2006b).

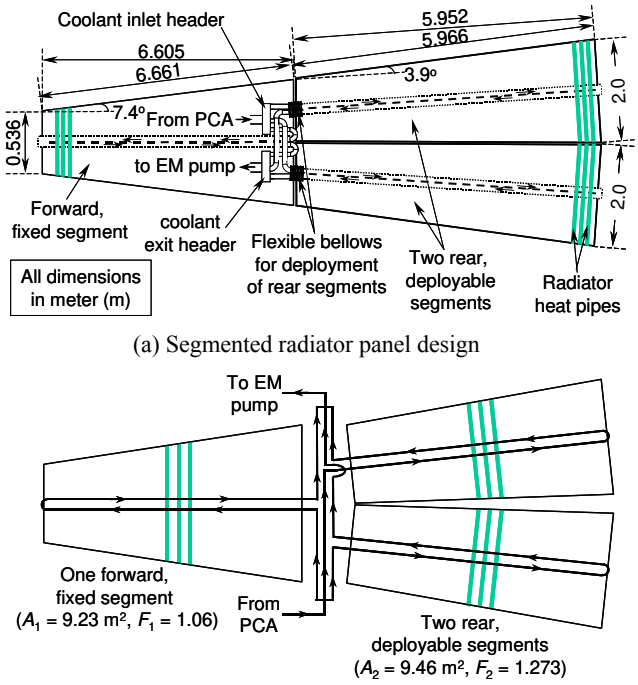

Fig. 17 Design and layout of segmented radiator panel.

system (Fig. 19) fits in the fairing envelop of the DELTA-IV Heavy launch vehicle, configured in a dual-manifest arrangement (El-Genk and Tournier, 2006b; Tournier and El-Genk, 2005 and 2006). When the radiator is fully deployed (Figs. 16 and 19), the radiation shadow shield protects system components within the radiator cavity and the payload from the reactor's neutrons and high-energy gammas.

To decrease the pressure losses and the liquid metal coolant inventory in the radiator and the secondary loops, hence the specific mass of the radiator, the 3 segments in each of the 6 radiator panels operate hydraulically in parallel (Fig. 17). Each segment has a perforated divider between the inlet and exit channels of the circulating liquid metal coolant (Fig. 18). The sensible heat is removed from the circulating coolant in the radiator segments and rejected into space using rubidium heat pipes with Carbon-Carbon (C-C) fins and armor (Fig. 20). The C-C armor protects the heat pipes against meteoroids impacts and the C-C fins increase the surface area for heat rejection. The heat pipes in the segments of the radiator panels are placed perpendicular to the liquid metal flow in the inlet and coolant circulation channels (Figs. 17 and 18). The baseline radiator panel design in Fig. 17 capitalizes on demonstrated operation and lifetime of liquid metal heat pipes during the SP-100 program (Rovang *et al*., 1991; Josloff *et al*., 1994; Marriott and Fujita, 1994; Juhasz & Rovang, 1995).

4.1 Design Optimization of Radiator Heat Pipes

The radiator of the space reactor power system in Fig. 16, with 6 forward radiator segments and 12 deployable rear segments, has an effective surface area of 203 m^2 and a total heat rejection rate of ~ 2.5 W_{th}. Each radiator panel has a multitude of rubidium (Rb) heat pipes of varying length (Fig. 20). The Rb heat pipes were designed to operate nominally at or below 2/3 of the prevailing sonic and/or capillary limit. Investigated were the effects on the radiator's specific mass and liquid lithium inventory in the secondary loop for the panels of: (a) having an equal heat rejection by the 6 forward segments and the 12 rear deployable segments of the radiator, and maintaining a total pressure loss of 12 kPa in the circulating lithium coolant in channels in each panel; (b) thermal-hydraulically operating the three segments of each panel in parallel; and (c) using perforated dividers between the circulating lithium in inlet and exit channels of the radiator segments.

Global Digital Central
ISSN: 2155-658X

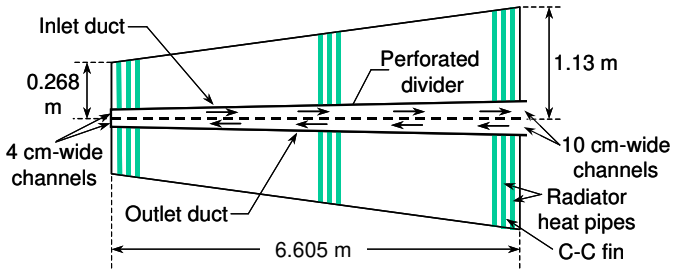

(a) Forward, fixed radiator panel segment (1 of 6)

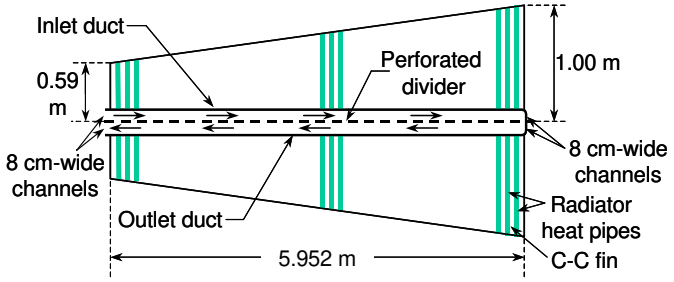

(b) Rear, deployable radiator panel segment (1 of 12)

Fig. 18 Radiator segments with perforated dividers (not to scale).

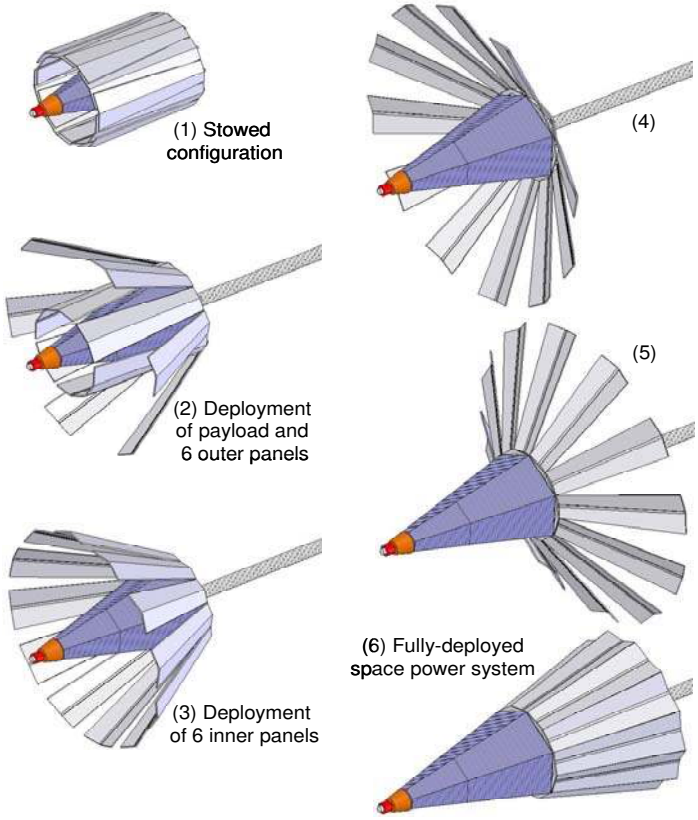

Fig. 19 Deployment sequence of the heat pipes radiator panels.

The orifices in the dividers are 1.0 mm in diameter, but their number density increases in the direction of the lithium flow.

The longest and shortest heat pipes in the fixed forward segments of the radiator panels are 1.13 m and 0.268 m long, while those in the rear, deployable segments of the panels are 1.0 m and 0.59 m long, respectively (Fig. 18). The length of the evaporator section of these heat pipes equals the width of one of the coolant channels. The rubidium heat pipes are protected against meteorites impact using ~ 2.0 mm thick C-C armor and are separated by C-C fins that are 0.5 mm thick and of varying width (Fig. 20).

The flat side of the Rb heat pipes provides good integration and thermal coupling to the circulating lithium channels (Fig. 20). The cross-section flow area of the vapor core is the same in all heat pipes (314.2 mm^2). It is comprised of a semi-circle of radius R_V and a rectangular section, H_V high and 2 x R_V wide. To minimize the heat pipes mass, the aspect ratio of the vapor space, $\alpha = H_V / (2\ R_V)$, is taken = 0.5 (Tournier and El-Genk, 2006). The Rb heat pipes have a 0.2 mm thick titanium (Ti) wick made of 3 layers of 150-mesh screen with an average pore radius of 50 μm. The wick volume porosity is 0.70 (Table 3). To decrease the liquid pressure losses in the Rb heat pipes, hence raising the capillary limit, the wick is separated from the 0.1 mm thick Ti liner (or wall) by a ~ 0.4 mm-thick annulus (Fig. 20b).

The radiator design was optimized for low mass and liquid lithium inventory, subject to the following operation and design constraints:

- Liquid lithium enters the radiator panels at 780 K, exits at 755 K;
- Total pressure drop in each radiator panel is 12 kPa;
- Design parameters of Rb heat pipes listed in Table 3;
- Rb heat pipes operate nominally at $\leq$ 2/3 of the prevailing sonic and capillary limits.
- All heat pipes are of an identical cross-section and C-C fins width and thickness, but different length (Table 3).

Table 3 Design parameters and materials of radiator heat pipes.

Parameter	Value
Vapor flow area per heat pipe (mm^2)	314.2
Aspect ratio, α	0.50
Radius of vapor space, R_V (mm)	9.38
Height of vapor space, H_V (mm)	9.38
Porous wick material / type	Ti / 150-mesh
Wick average porosity	0.70
Wick effective pore radius (μm)	50.0
Wick thickness (mm) / number of layers	0.20 / 3
Wall material / thickness (mm)	Ti / 0.10
C-C fin and armor density (kg / m^3)	1,800.
C-C fins thickness (mm)	0.5
C-C emissivity/ Space sink temperature (K)	0.90 /10

The optimization results of the radiator segments are listed in the last 2 columns in Table 4. Each of the rear deployable segments of the radiator panel employs 144 Rb heat pipes with a liquid annulus cross-sectional area of 27 mm^2. The longest heat pipes are 2.93-cm wide. The Li inlet and exit channels are 8 cm wide and 0.74 cm high (Table 4).

The lithium mass flow rate in and the heat rejection load of each of the rear deployable segments are 1.426 kg/s and 149.3 kW$_{th}$, respectively. Each forward, fixed segment of the radiator has 120 Rb heat pipes with a liquid annulus, 34 mm^2 in cross-sectional area, to ensure that the longest heat pipes operate nominally at 2/3 of the capillary limit. The Rb heat pipes in the forward fixed segments are not sonic limited. However, decreasing the number of heat pipes increases the C-C fin width beyond 4.29 cm, and decreases the heat rejection capability of fixed segments of the radiator below 115.3 kW$_{th}$, ~ 23% lower than that (149.3 kW) of the deployable segments.

4.2 Radiator Heat Pipes Performance

Since the evaporator length (L_{ev} = 0.15 m) is only 10% of the total length of the Rb heat pipes and the heat input to the heat pipe is applied to the flat side of the evaporator (Fig. 20), the temperature drop across the evaporator structure is much larger than that in the condenser. To calculate these temperature drops, the UNM-HP model (El-Genk and Tournier, 2004b) accounts for the circumferential heat transport in the highly conductive C-C armor (its circumferential thermal conductivity varies between 240 and 200 W/m.K in the temperature range from 600 K to 800 K). The model assumes a 10 K temperature drop between the condenser wall and the root of the C-C fins of the Rb heat pipes. Lateral

Global Digital Central
ISSN: 2155-658X

Table 4 Performance results of the heat pipe radiator panels with different design features*.

Parameter	Single radiator panel	Without perforated dividers		With perforated dividers	
		Forward, fixed segment	Rear, deployable segments	Forward, fixed segment	Rear, deployable segments
Geometrical					
Number	1	1	2	1	2
Physical surface area (m^2)	27.18	9.23	9.46	9.23	9.46
Effective radiation view factor	1.211	1.06	1.273	1.06	1.273
Length (m)	12.52	6.605	5.952	6.605	5.952
Height of flow channel (cm)	2.95	1.30	1.51	0.74	1.145
Orifice diameter (mm)	-	-	-	1.0	1.0
Orifices number density (#/cm^2)	-	-	-	2.4 – 4.0	0.86 – 11.3
Shortest heat pipe length (cm)	26.8	26.8	59.0	26.8	59.0
Longest heat pipe length (cm)	190.3	113.0	100.0	113.0	100.0
Shortest heat pipe evaporator (cm)	8.0	8.0	8.0	4.0	8.0
Longest heat pipe evaporator (cm)	16.0	8.0	8.0	12.0	8.0
Number of heat pipes	456	120	144	120	144
C-C fin width / thickness (cm)	1.47/ 0.05	4.29/ 0.05	2.93 / 0.05	4.29 / 0.05	2.93 / 0.05
Liquid annulus in heat pipes (mm^2)	70.0	34.0	27.0	34.0	27.0
Annular gap in heat pipe (mm)	0.974	0.485	0.387	0.485	0.387
Heat pipe C-C wall thickness (mm)	2.10	1.94	1.94	1.94	1.94
Lithium coolant volume (liters)	88.4	13.68	14.32	7.79	10.86
Performance parameters					
Lithium flow rate (kg/s)	4.0	1.07	1.444	1.10	1.426
Heat rejection load (kW_{th})	419.4	112.0	151.3	115.3	149.3
Dry mass (kg)	291.1	49.30	59.39	49.09	59.27
Dry sp. mass (kg/m^2)/ power (kW_{th}/kg)	10.71 / 1.44	5.34 / 2.27	6.28 / 2.55	5.32 / 2.35	6.26 / 2.52
Panel flow rate (kg/s)	4.0	3.96		3.95	
Panel heat rejection (kW_{th})	419.4	414.6		413.9	
Panel dry mass (kg)	291.1	168.1		167.6	
Coolant mass in panel (kg)	42.9	20.54		14.32	
Coolant volume in panel (liters)	88.4	42.33		29.50	
Panel total mass (kg)	334.0	188.6		182.0	
Panel specific mass (kg/m^2)	12.29	6.70		6.46	
Panel specific power (kW_{th}/kg)	1.26	2.20		2.27	

(*) Calculations are for the same pressure drop (12 kPa) and lithium inlet and exit temperatures of 780 K and 755 K, respectively.

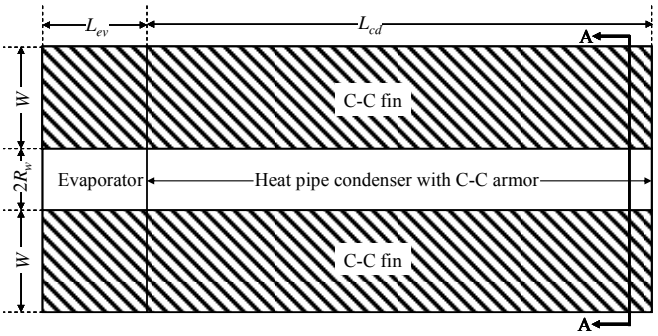

(a) Longitudinal view (not to scale)

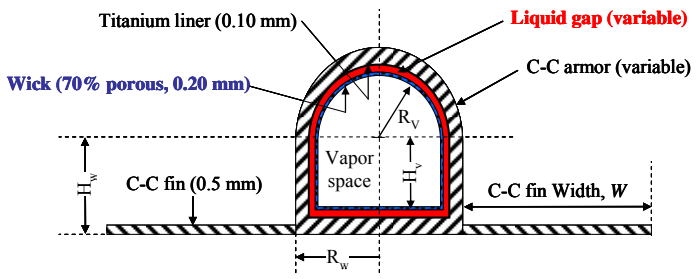

(b) Cross-sectional view A – A

Fig. 20 Radiator heat pipe with C-C armor and fins.

heat conduction in the C-C fins, perpendicular to the heat pipes, is accounted for, but neglected along the fin length since the fin length is more than 27 times its width (up to 5.5 cm). The results of the effects of using different liquid-metal working fluids for the radiator heat pipes are discussed next.

The calculated operation limits of radiator K, Rb and Cs heat pipes are shown in Figs. 21a, b and c, respectively. Since potassium has the highest FOM, but the lowest vapor pressure, the capillary limit is very high. However, the sonic limit is most limiting (Fig. 21a). Therefore, at nominal operation of the K heat pipe, the vapor Mach number at the evaporator exit is kept equal to 0.40 (i.e., the nominal power throughput of the radiator K heat pipe equals 40% of the sonic limit. The operation limits of the Rb radiator heat pipe are shown in Fig. 21b. Rubidium's vapor pressure is higher than that of potassium and its sonic limit is higher. However, the FOM of rubidium is < half that of potassium (Figs. 1 and 2). The operation of the Rb heat pipes is constrained by the capillary limit at temperatures > 762 K, and by the sonic limit below 762 K (Fig. 21b). The nominal power throughput equals 40% of the sonic limit below 762 K, and 40% of the capillary limit above 762 K, which explains the inflection point in the nominal operation curve for the Rb heat pipe at 762 K (Fig. 21b).

The operation limits of the radiator Cs heat pipe are shown in Fig. 21c. Cesium has a slightly higher vapor pressure than Rb (Fig. 2); however, the FOM of Cs is 33% lower, thus the capillary limit of the Cs heat pipe is lower than that of the Rb heat pipe. As a result, the temperature range over which the capillary limit prevails is wider for the Cs heat pipes (above 724 K), and the nominal operation is limited by the sonic limit below 724 K (Fig. 21c).

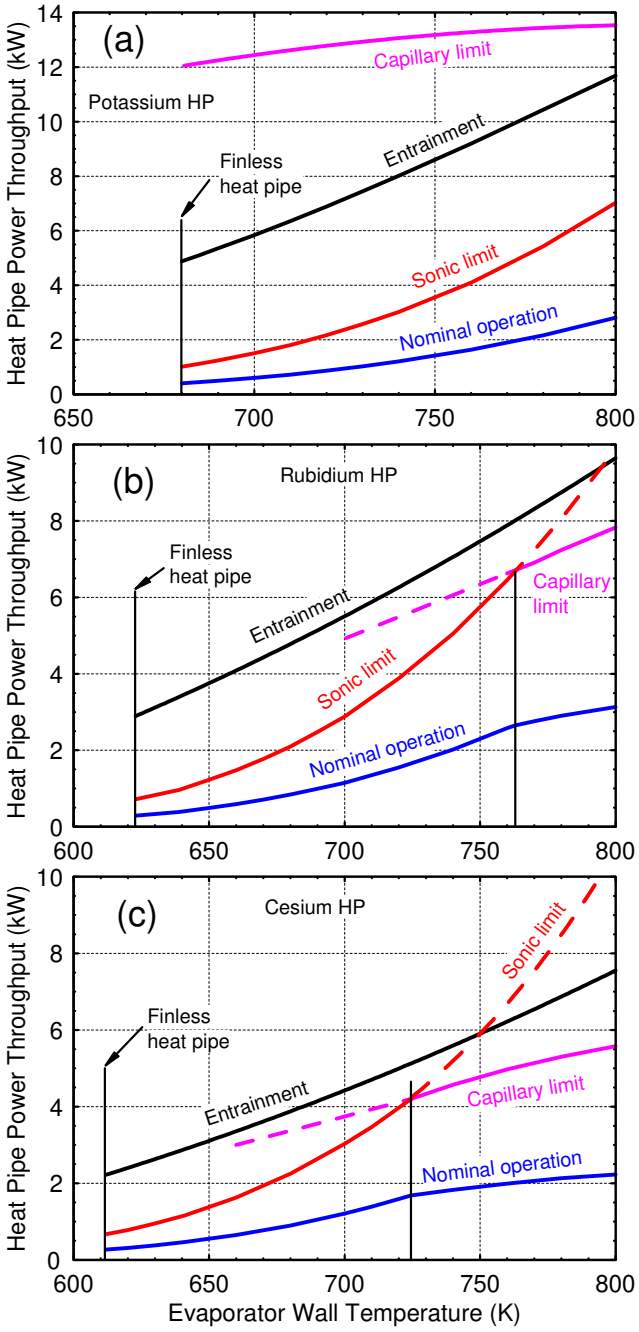

Fig. 21 Operation limits and power throughputs of potassium, rubidium, and cesium radiator heat pipes.

The nominal power throughputs of the 3 alkali metal radiator heat pipes are compared in Fig. 22a as functions of evaporator temperature. At evaporator wall temperatures < 724 K, the Cs heat pipe transports the highest power, with the Rb heat pipe a very close second. This is because Cs has the highest vapor pressure of the alkali metals considered (Fig. 2). Above 724 K, the Rb heat pipe transports the highest power. At these temperatures, the Cs heat pipe has the lowest FOM (Fig. 1) and is subject to the capillary limit. Above 780 K, the K heat pipe transports more power than the Cs heat pipe, and could transport more power than the Rb heat pipe at evaporator wall temperatures > 810 K (Fig. 22a). At these temperatures, potassium has the highest FOM of all these fluids.

The nominal temperature drops along the radiator alkali-metal heat pipes are compared in Fig. 22b. These temperature drops include those through the evaporator and condenser structures, comprised of the C-C wall and metallic liner, the liquid gap and the porous wick, and in the vapor along the heat pipe. While the conduction temperature drops increase proportionally with the power throughput, the vapor temperature drop is a function of the vapor pressure (or temperature), the vapor Reynolds number, and the power throughput. When the heat pipe operates at Ma = 0.4 and the vapor flow is turbulent, the vapor temperature drop along the heat pipe is small: 14 K, 12.8 K and 12.5 K for the K, Rb and Cs heat pipes, respectively.

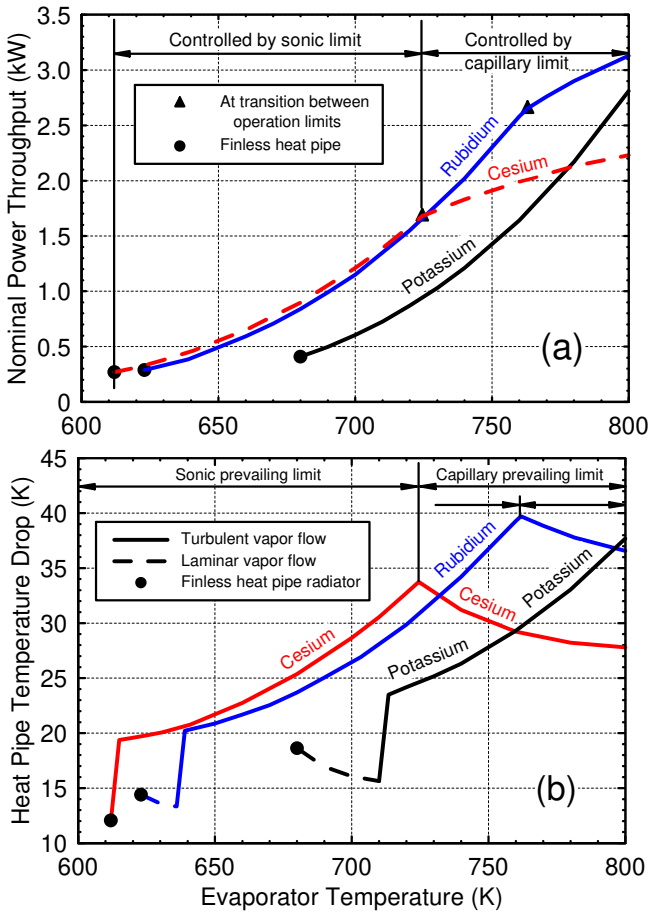

Fig. 22 Comparison of power throughputs and temperature drops.

Table 5 Design parameters and materials of radiator heat pipes.

Parameter	Value
Heat pipe evaporator length (m)	0.15
Heat pipe condenser length (m)	1.35
Heat pipe total length (m)	1.50
Vapor flow area (mm^2)	314.2
Heat pipe aspect ratio, α	0.50
Radius of vapor space, R_V (mm)	9.38
Height of vapor space, H_V (mm)	9.38
Porous wick material / type	Ti / 400-mesh
Wick average porosity	0.70
Wick effective pore radius (μm)	19.0
Wick thickness (mm) / number of layers	0.20 / 4
Liquid gap flow area (mm^2)	25.0
Liquid gap thickness (mm)	0.359
Liner material / thickness (mm)	Ti / 0.10
C-C armor thickness (mm)	1.944
C-C fin and armor density (kg / m^3)	1,800.
Thickness of C-C fins (mm)	0.5
C-C emissivity	0.85
Radiator's effective view factor (*)	1.30
Space sink temperature (K)	10

(*) Assuming radiation from top and bottom surfaces.

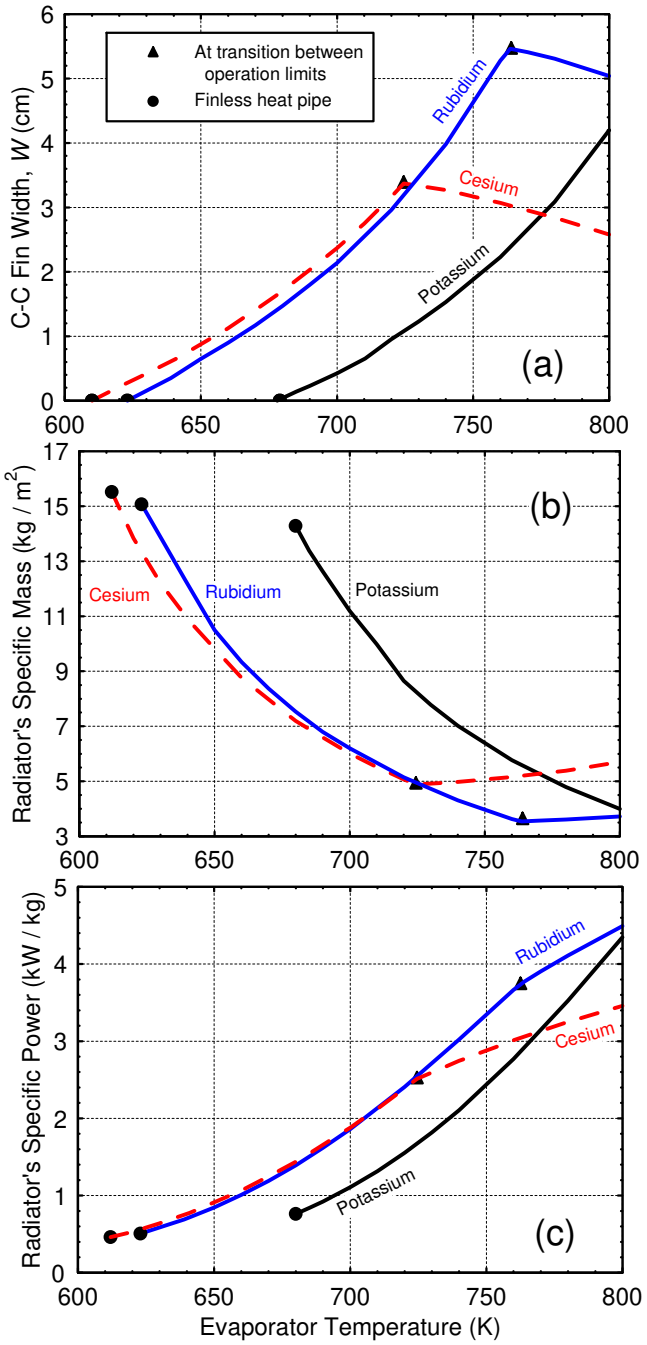

Fig. 23 Performance comparison of the radiators potassium, rubidium and cesium heat pipes.

The temperature drops along the heat pipes increase as the evaporator temperature increases (Fig. 22b), up to their maximum values of 39.6 K and 33.5 K for the Rb and Cs heat pipes, respectively. When the heat pipe's operation is capillary limited, but with a 60% design margin, the vapor temperature drop decreases rapidly with increasing temperature. This is because the vapor pressure increases, while the Mach number decreases, with increasing evaporator temperature. As a result, the total temperature drops along the Rb and Cs heat pipes decrease with increasing evaporator wall temperature beyond 762 K and 724 K, respectively (Fig. 22b). The sharp increase in the vapor temperature drop at low temperature corresponds to when vapor flow transitions from laminar to turbulent.

The width of the C-C fins for rejecting the thermal power to space is shown in Fig. 23a, and the specific mass and power of the radiator section with one heat pipe are shown in Figs. 23b and 23c. Using a C-C fin thickness > 0.5 mm actually degrades the performance of the radiator heat pipes. In the temperature range where sonic is the prevailing limit, the required C-C fin width increases with increasing the power throughput (Fig. 23a). When the operation of the Rb and Cs heat pipes is capillary limited, the radiation heat flux increases faster with increasing temperature than the capillary limit of the heat pipe, and the required fin width decreases with increasing temperature (Fig. 23a).

As shown in Fig. 23b, the Cs heat pipes radiator has the lowest specific mass up to an evaporator wall temperature of 724 K, below which the power throughput is constrained by the sonic limit. Above this temperature, and up to ~ 800 K, the Rb heat pipe radiator has the lowest specific mass, because of the higher FOM of rubidium (Fig. 1). The densities of liquid K, Rb and Cs at 700 K are 742 kg/m^3, 1300 kg/m^3 and 1610 kg/m^3, respectively. As a result, the Cs heat pipe is the heaviest (0.580 kg), followed by the Rb heat pipe (0.563 kg), then the K heat pipe (0.534 kg). Fig. 23b shows that the specific masses of the K and Rb heat pipe radiators are almost identical at 800 K, even though the latter has wider C-C fins (5 cm compared to 4.2 cm, Fig. 23a).

The specific power (in kW/kg) of the Cs heat pipes radiator increases rapidly with increasing temperature, as the vapor pressure increases exponentially (Fig. 2). Below 660 K, the specific power of the Cs heat pipe radiator is $\leq$ 1 kW/kg and its specific mass $\geq$ 9 kg/m^2 (Figs. 23b and 23c). The former increases to 2.5 kW/kg and the latter decreases to 5 kg/m^2 as the evaporator wall temperature increases to 724 K. Above 724 K, the Rb heat pipes radiator has the best performance, with a specific mass < 5 kg/m^2 and a specific power > 2.5 kW/kg (Figs. 23b and 23c). Above 800 K, the radiator with the K heat pipes performs the best, with a specific mass < 4 kg/m^2 and a specific power > 4.4 kW/kg. The present study is not entirely fair to the K heat pipes radiator, since they would not require such a thick liquid gap, (Fig. 1). Nevertheless, the results are indicative of the preferential domain of operation of the radiator heat pipes with different alkali-metal working fluids. The Cs heat pipes radiator, with C-C fins and armor, performs best at 680 – 720 K. The Rb heat pipes radiator is better at higher temperatures, 720 – 800 K. At evaporator wall temperatures > 800 K, the low vapor pressure of potassium is no longer an issue, and the K heat pipes radiator is the best performer and lightest.

5. SCALABLE AMTEC INTEGRATED REACTOR POWER SYSTEM (SAIRS)

Heat pipes have also been considered for cooling space nuclear reactors (Angelo and Buden, 1985; Ranken, 1982 and 1990; Determan and Hagelston, 1992; Poston *et al*., 2002; Ring *et al*., 2003; Tournier and El-Genk, 2004; El-Genk and Tournier, 2004a; El-Genk 1994, 2008a). An example is demonstrated in the conceptual design of the 110 kWe, Scalable AMTEC Integrated Reactor Space Power System (SAIRS) (El-Genk and Tournier, 2004a; El-Genk, 2008a). This power system employs a fast-spectrum reactor that is cooled using Na heat pipes, and a C-C armored, potassium (K) heat pipes radiator. Figure 24a presents an isometric view of the fully integrated SAIRS and Fig. 24b is a cross-section view of the arrangement of the Alkali Metal Thermal to Electric conversion (AMTEC) units, showing the thermal coupling to the reactor's Na heat pipes and the panels of radiator K heat pipes. Details on the description of the AMTEC unit design and performance are outside the scope of this paper, but could be found elsewhere (El-Genk and Tournier, 2004a).

SAIRS-C employs 18, 6.17 kWe Na-AMTEC units grouped in six blocks (Fig. 24b). Each block consists of 3 AMTEC units serviced by 10 reactor Na-heat pipes and has a separate K heat pipes radiator panel. The AMTEC units are placed behind the radiation shadow shield within the radiator cavity (Fig. 24a).

SAIRS fast-spectrum nuclear reactor is cooled by 60, 1.5 cm OD Mo-14%Re / sodium heat pipes of varying length. After exiting the Mo-14%Re reactor vessel (0.5-mm thick) and the rear BeO axial reflector (4-cm thick), the reactor Na-heat pipes are bent around the radiation shadow shield and then laid out inside the radiator cavity, where they are conductively coupled to the Mo-41%Re evaporator

walls of the AMTEC units (Fig. 24). The sections of the Na-heat pipes extending from the reactor to the AMTEC unit blocks are thermally insulated using Multi-Foils Insulation (MFI) comprised of 25, 10 μm thick Mo foils separated by 100-μm gap.

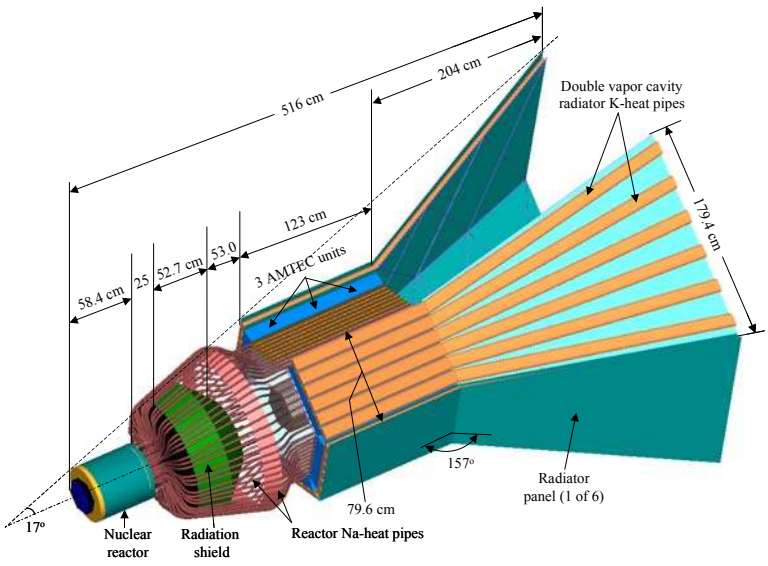

(a) Three-dimensional view of SAIRS-C

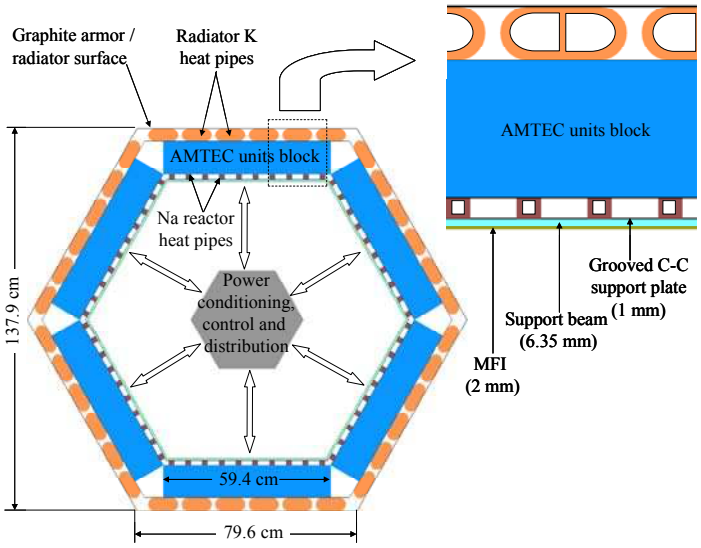

(b) Cutaway view through converters' section

Fig. 24 Isometric and cross-sectional views of SAIRS-C space reactor power system (El-Genk and Tournier, 2004a).

The Mo-14%Re porous wick (0.2 mm thick) is separated from the Mo-14%Re wall of the reactor Na-heat pipes by a 0.6 mm liquid annulus (Fig. 25). This annulus decreases the liquid pressure losses and hence, raises the wicking limit of the heat pipes. The porous wick has an average porosity of 0.69 and 18 μm effective pore radius. The length of the evaporator in the Na-heat pipes is identical to the active height of the reactor core (42 cm), and that of the condenser section is equal to the length of a block of AMTEC units, 1.23 m (Fig. 25 and Table 6). The length of the adiabatic section varies by up to ~10 cm, depending on the radial location of the heat pipe in the reactor core. The longest Na heat pipe has a 1.84 m long adiabatic section (Table 6).

Each radiator panel has two sections that are thermally coupled using six, double vapor cavity K-heat pipes (Fig. 24). The front (or evaporator) section is a flat rectangle that spans the length of the AMTEC units block and rejects heat to space from its outer surface. The inner surface of this radiator panel section is conductively coupled to the condensers of the AMTEC units. The rear (or condenser) section of the radiator panel is trapezoidal and rejects heat to space from its outer and inner surfaces. It is angled ~157° relative to the front section but remains within the system's cone angle (34°). The width of the C-C fins of the 6 K-heat pipes is constant in the front section, but increases with distance along the rear section (Fig. 24a).

There are 60 fuel modules in the SAIRS reactor core (Fig. 25). Each module consists of three uranium nitride (UN), Re-clad fuel pins arranged in a triangular lattice (Fig. 25) and single Na heat pipe. The cladding along the active length of the fuel pins (0.42 m) is brazed to a Mo-14%Re / Na heat pipe having a 0.4 mm thick wall and an outer diameter of 1.5 cm, same as that of the fuel pins.

Table 6 Design and performance of reactor Na heat pipes in SAIRS.

Parameter/subsystem	SAIRS-A (Low-T)	SAIRS-C (Low mass)
Reactor Heat Pipe Design:		
Heat pipes working fluid	Sodium	Sodium
Volume porosity of heat pipe wick	0.69	0.69
Effective pore radius of wick (μm)	9.0	18.0
Vapor core radius (mm)	6.30	6.30
Porous wick thickness (mm)	0.20	0.20
Liquid annulus (mm)	0.60	0.60
Mo-14% Re wall thickness (mm)	0.40	0.40
Heat pipe OD (mm)	15.0	15.0
Evaporator length (m)	0.42	0.42
Adiabatic section length (m)	1.90	1.84
Condenser length (m)	1.64	1.23
Longest Na- heat pipe (m)	3.96	3.49
Nuclear Reactor:		
Total number Na- heat pipes	60	60
Thermal power (kW)	487.7	407.3
Radial peaking factor	1.27	1.27
Average Na-heat pipe:		
Power throughput (kW)	7.93	6.62
Evaporator wall temperature (K)	1133.4	1202.4
Condenser wall temperature (K)	1112	1189
Prevailing operation limit (kW)	17.0 (cap)	14.9 (cap)
Total temperature drop (K)	21.4	13.4
Vapor temperature drop (K)	9.0	2.0
Evaporator/ Condenser structure (K)	9.9 / 2.5	8.5 / 2.9
Vapor Mach number at evaporator exit	0.108	0.049
Peak power Na- heat pipe:		
Power throughput (kW)	10.07	8.41
Evaporator wall temperature (K)	1141.0	1206.5
Total temperature drop (K)	29.0	17.5
Vapor temperature drop (K)	13.2	2.9
Evaporator/ Condenser structure (K)	12.6 / 3.2	10.9 / 3.7
Vapor Mach number at evaporator exit	0.132	0.061
Average next to failed heat pipe:		
Power throughput (kW)	10.57	8.82
Evaporator wall temperature (K)	1142.8	1207.5
Total temperature drop (K)	30.8	18.5
Vapor temperature drop (K)	14.3	3.2
Evaporator/ Condenser structure (K)	13.2 / 3.3	11.4 / 3.9
Vapor Mach number at evaporator exit	0.138	0.064
Peak power next to failed heat pipe:		
Power throughput (kW)	13.42	11.21
Evaporator wall temperature (K)	1153.8	1213.2
Total temperature drop (K)	41.8	24.2
Vapor temperature drop (K)	20.7	4.8
Evaporator/ Condenser structure (K)	16.8 / 4.3	14.5 / 4.9
Vapor Mach number at evaporator exit	0.167	0.080

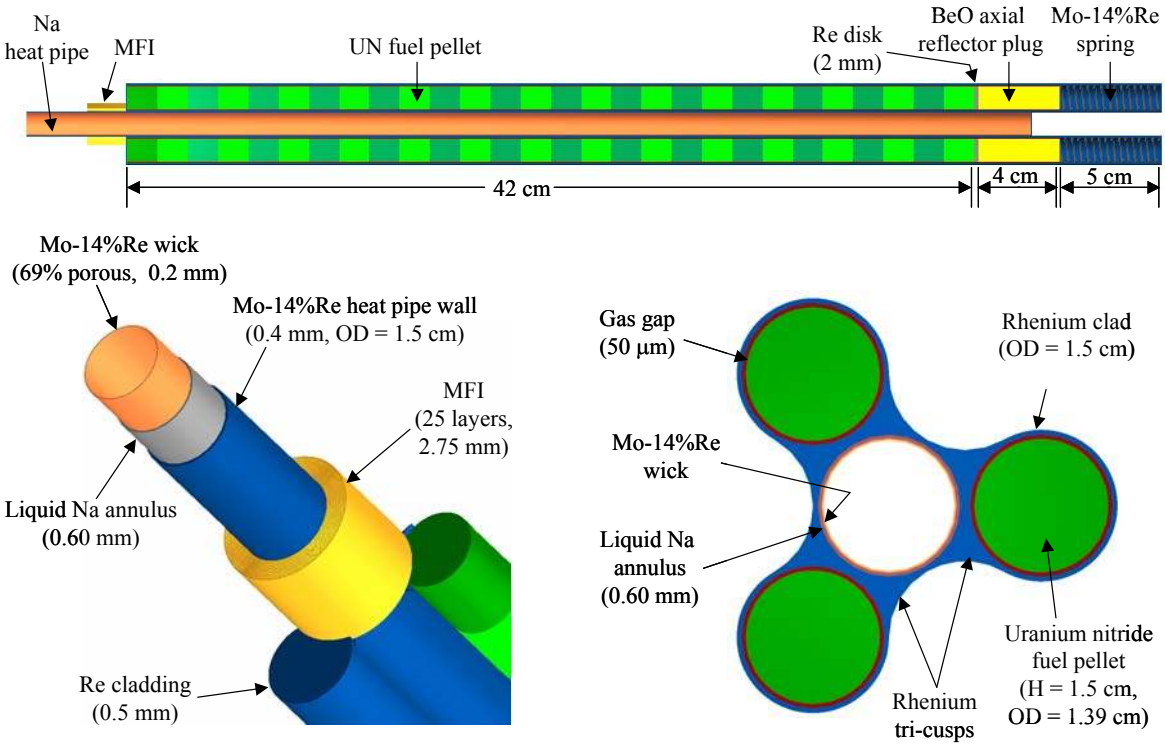

Fig. 25 Cross section and isometric views of a heat pipe fuel module in SAIRS reactor.

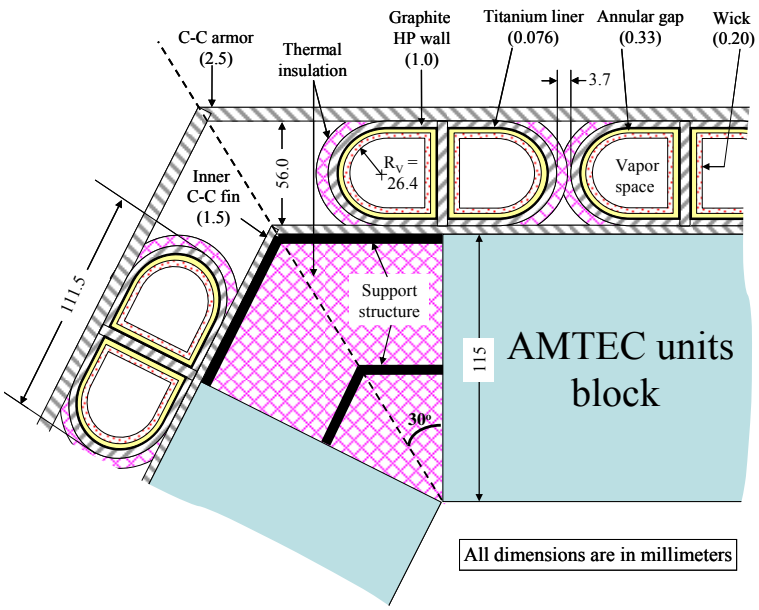

Fig. 26 A cutaway view of radiator potassium heat pipes in SAIRS-C.

5.1 Performance of SAIRS Potassium Heat Pipes Radiator

The performance of the radiator K heat pipes is investigated for two power system options; one for operating at the lowest hot side temperature (SAIRS-A) and the other with the lowest mass (SAIRS-C) (Table 7). Figure 26 presents a cutaway view showing the design details of the radiator K-heat pipes and the layout of their C-C armor. Each radiator K-heat pipe has a thin titanium liner (0.0762 mm thick) encased in a 1.0 mm-thick C-C outer wall, and a 0.2 mm-thick titanium wick (with an effective pore radius of 38.1 μm) separated from the titanium liner by a 0.33 mm liquid annulus (Fig. 26, Table 7). The vapor flow area in the K-heat pipes ensures that at an evaporator wall temperature of 686 K, corresponding to an AMTEC condenser temperature of 700 K, the heat pipes operate at < 30 % of the sonic limit (for > 70% operation margin). Such large design margin also ensures that in case of a failure of up to two adjacent K-heat pipes, the neighboring K-heat pipes will operate at < 60% of the sonic limit. All the design and performance analyses of the reactor Na-heat pipes and the radiator K-heat pipes were performed using UNM-HP, described earlier.

The sonic, capillary, and the entrainment limits of the radiator K-heat pipes are calculated at a nominal evaporator wall temperature of 686 K. In SAIRS-C, the vapor pressure drop in the K heat pipes evaporator section is highest and the design margin to the sonic limit is lowest, but still acceptable. The length of the evaporator section for the radiator K-heat pipes in contact with the AMTEC blocks is 1.23 m and the total length of the radiator K-heat pipes is 3.44 m (Table 7). Figure 27 compares predictions of the operation limits of the K heat pipes with those obtained using HTPIPE (Woloshun *et al*., 1989). The performance results of the K heat pipes for the radiator panels in SAIRS-A are compared with those in SAIRS-C in Table 7.

Figure 27 indicates that the predictions of the sonic and the capillary or wicking limits by the two models are in good agreement. However, the entrainment limits predicted by HTPIPE are about 3 times those calculated by UNM-HP. Nonetheless, the results in Fig. 27 indicate that at the nominal operating temperature (marked by a solid circle symbol), the entrainment limit for the radiator K-heat pipes in SAIRS-C is very high and thus, of no concern. The evaporator wall temperature (686 K) of the point design of the K-heat pipes falls near the intersection of the capillary/wicking limit and the sonic limit. The later is the constraining limit for the K-heat pipes in SAIRS-C.

5.2 Point Design of Sodium Heat Pipes in SAIRS-A Reactor

In the SAIRS-A reactor, each Na-heat pipe carries on average 7.93 kW of thermal power. These heat pipes are 3.96 m-long, have 1.9 m-long adiabatic section and use a porous wick with an average pore radius of 9 μm. The operation limits for these heat pipes are calculated assuming uniform heat input and heat removal along their evaporator and condenser sections.

Global Digital Central
ISSN: 2155-658X

Table 7 Design and performance of SAIRS radiator K-heat pipes.

Parameter/subsystem	SAIRS-A (Low-T)	SAIRS-C (Low Mass)
Radiator Heat Pipe Design:		
Heat pipe working fluid	potassium	potassium
Volume porosity of wick	0.69	0.69
Effective pore radius of wick (μm)	38.1	38.1
Vapor flow area of single cavity (cm^2)	32.0	25.0
Ti porous wick thickness (mm)	0.20	0.20
Liquid annulus (mm)	0.36	0.33
Ti liner thickness (mm)	0.076	0.076
C-C wall thickness (mm)	1.0	1.0
Height of heat pipe (cm)	7.07	5.6
Width of double-cavity heat pipe (cm)	11.49	11.15
Evaporator length (m)	1.64	1.23
Condenser length (m)	2.51	2.21
Total length of heat pipe (m)	4.15	3.44
Design and Performance of C-C Fin:		
Thickness of inner C-C fin/armor (mm)	1.6	1.5
Thickness of outer C-C fin/armor (mm)	2.7	2.5
AMTEC/evaporator wall loss (K)	14	14
Heat pipe wall/fin contact loss (K)	8	8
Effective surface emissivity	0.85	0.85
Space sink temperature (K)	250	250
Performance of Single-Cavity Heat Pipe:		
Power throughput (kW)	4.89	3.83
Evaporator wall temperature (K)	686	686
Temperature drop in vapor (K)	6.5	6.7
Temperature drop in structure (K)	9.2	9.4
Total temperature drop (K)	15.7	16.1
Prevailing capillary limit (kW)	13.82	11.43
Sonic limit (kW)	17.7	13.4
Vapor Mach number at evaporator exit	0.276	0.286

The sonic limit at the end of the adiabatic section is always lower than at the exit of the evaporator section, thus it is the prevailing operation limit when the temperature of the Na vapor temperature at the exit of the evaporator section is < 1050 K (Fig. 28). The sonic limit is reached first at the end of the adiabatic section, as the vapor pressure and density decrease steadily with the increase in the vapor friction pressure losses along this section. The vapor mass flow rate remains constant and equal to that at the exit of the evaporator section. At higher temperatures, the capillary limit is lower than the sonic limit, thus becoming the prevailing operation limit of the reactor Na-heat pipes.

The third operation limit of the entrainment of the liquid in the counter-current vapor flow decreases the amount of the liquid Na returning from the condenser that reaches the evaporator section. As shown in Fig. 28, the entrainment limit is lower than the sonic limit at the exit of the evaporator section when the vapor temperature > 1030 K, but is much higher than the capillary limit. The boiling limit that occurs at very high temperatures is not a concern because the peak liquid Na superheat at the mid-plane of the evaporator section is < 13 K. This liquid superheat is too low to ensue boiling of the highly conductive liquid sodium on the inside surface of the heat pipe wall.

The sizing and performance optimization of the Na-heat pipes in SAIRS are based on a reactor nominal thermal power of 488 kW_{th}, or an average power throughput per heat pipe of 7.93 kW (Table 6). With the calculated fuel pin peak-to-average power ratio in the reactor core = 1.27 (King and El-Genk, 2004), the Na heat pipe at the location of the peak power in the reactor core transports 10.07 kW. This value increases by 1/3 to 13.42 kW for the heat pipe adjacent to a fuel module in which the Na-heat pipe failed. These values of the operation power throughput for the reactor Na-heat pipes are indicated in Fig. 28 by the solid circle symbols. The operation margin for these Na heat pipes is 21% at the highest power throughput (13.42 kW), compared to the

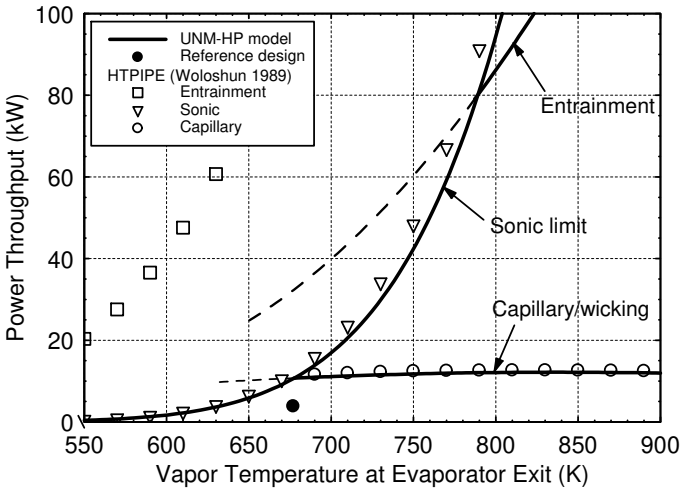

Fig. 27 Operation limits of potassium heat pipes in SAIRS-C radiator.

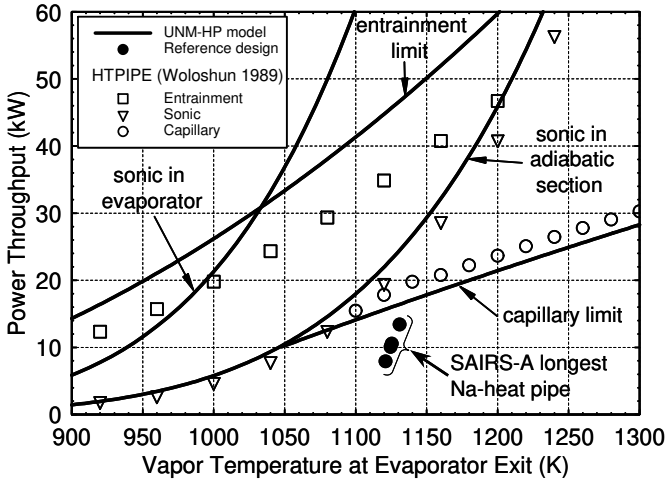

Fig. 28 Limits of longest sodium heat pipe in SAIRS-A reactor.

wicking limit (17 kW), and as much as 53% for the average heat pipe in the reactor core. The average reactor core temperature in SAIRS-A is 1133 K, only 41 K higher than that of the hot side of the AMTEC units.

6. S^4-CBC SPACE REACTOR POWER SYSTEM

A deployable, water heat pipes radiator design with 6 segmented panels has also been developed (El-Genk and Tournier, 2006a) for the Scalable, Submersible, Subcritical Safe (S^4) reactor power system with a gas-cooled reactor. The reactor core is divided into three hydraulically separate, but thermally and neutronically coupled sectors. Each reactor sector has a separate recuperated Closed Brayton Cycle (CBC) loop, with a turbo-machine unit for energy conversion (Gallo and El-Genk, 2009; El-Genk *et al*., 2010). Figure 29 presents a line diagram of one CBC loop in this power system. The reactor sectors are cooled by a circulating He-Xe gas mixture with a molecular weight of 40 g/mole. Figure 30 present a cross-sectional view of the S^4 reactor.

Each CBC loop is thermally coupled to a circulating liquid NaK-78 secondary loop for cooling the gas working fluid before returning to the compressor of the turbo-machine unit (Fig. 29). The NaK loop employs a pair of water heat pipes radiator panels that operate hydraulically in parallel. The radiator panels remove the waste heat from the circulating NaK in the secondary loop and reject it into space. The radiator's water heat pipes have C-C armor and integrated fins. The NaK flow ducts in the radiator panels are also armored. Each radiator panel has three segments that operate in parallel to reduce the NaK inventory in the radiator ducts and the secondary loop. The NaK enters and exits the water heat pipe radiator segments at 530 K and 395 K, respectively.

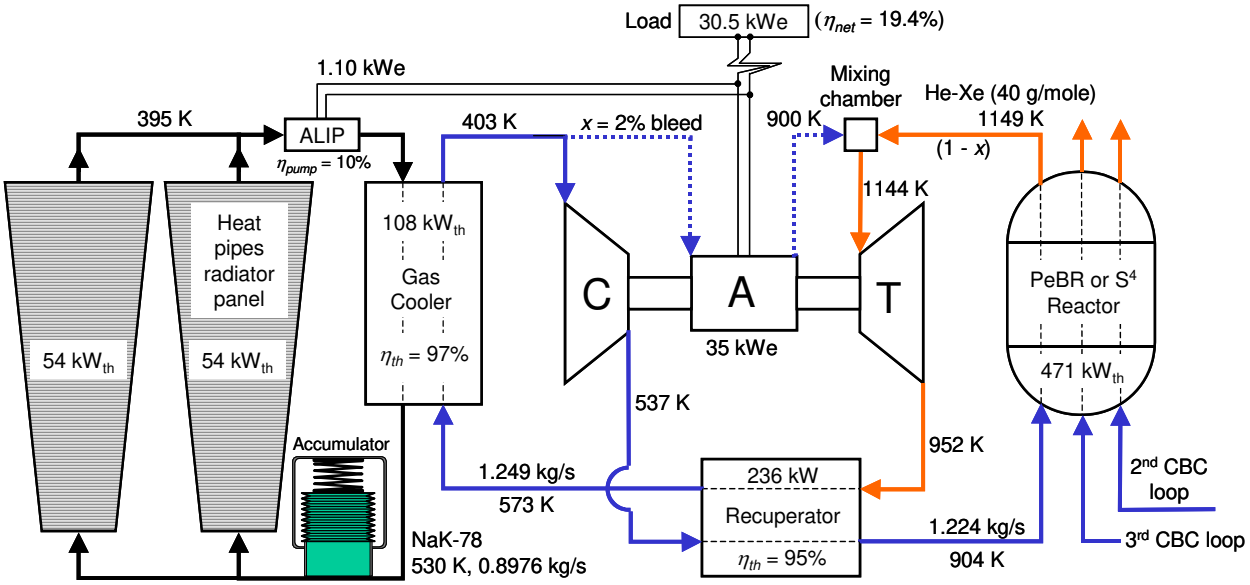

Fig. 29 Operation parameters of S^4 reactor power system with 3 CBC loops (El-Genk and Tournier, 2006a; Gallo and El-Genk, 2009).

Each turbo-machine in the S^4-CBC reactor power system delivers a net electric power to the load of 30.5 kWe, after accounting for 10% transmission and inversion losses (Fig. 29). Each radiator panel nominally rejects 54 kW$_{th}$ and the He-Xe gas cooler in each CBC loop has an efficiency of 97%. The total thermal power removed from the reactor sectors is 471 kW$_{th}$ at nominal inlet and exit temperatures of 904 K and 1149 K. Each CBC loop has a recuperator with an efficiency of 95% and a net thermal efficiency of 19.4% (Fig. 29). The liquid NaK in the secondary loops is circulated using Alternative Linear Induction Pumps (ALIPs) powered by a fraction of the electrical power generated by the CBC turbo-machines. The He-Xe gas mixture working fluid enters the CBC compressors at 403 K and exits at 537 K. Two percent of the gas flow is bled upstream of the compressor to cool the bearings and the rotor of the electrical alternator. At the entrance to the turbine, the bleed gas is mixed with that exiting the reactor at 1149 K. The circulating liquid NaK secondary loops are equipped with accumulators to accommodate the changes in the liquid NaK volume during transient operation, and control its pressure in the secondary loops.

6.1 Design of Water Heat Pipes and Radiator Panels

The design and layout of the deployable radiator panels for the S^4-CBC space power system (El-Genk and Tournier, 2006a; El-Genk, 2008b; Gallo and El-Genk, 2009) are identical to those described earlier (Fig. 19). Heat is removed from the circulating NaK in the ducts of the radiator panels and rejected into space by water heat pipes of varying lengths (Fig. 31). These heat pipes are laid at a right angle to the circulating NaK ducts. The longest and shortest heat pipes in the forward segments of the radiator panels are 1.13 m and 0.268 m long, while those in the rear, deployable radiator segments are 1.0 m and 0.59 m long. The lengths of the evaporator sections of the water heat pipes equal the width of the circulating NaK ducts. The flat side of the D-shaped water heat pipes provides good integration and thermal coupling to the NaK ducts (Fig. 31). Each forward radiator segment has 96 water heat pipes and each rear segment has 108 water heat pipes with connecting C-C fins that are 0.5 mm thick (Fig. 31). The radiator water heat pipes (Fig. 31b) have a C-C composite wall and a thin (0.1 mm thick) titanium liner, and integrated C-C fins of varying width. The C-C enclosure of the water heat pipe protects against meteorites impact and serves as a pressure boundary for the water working fluid. The cross-section flow area of the vapor flow in the heat pipes varies from 1.5 cm^2 to 4 cm^2. It is comprised of a semi-circle of radius R_V and a rectangular section that is H_V high and 2 x R_V wide (Fig. 31b). To minimize the

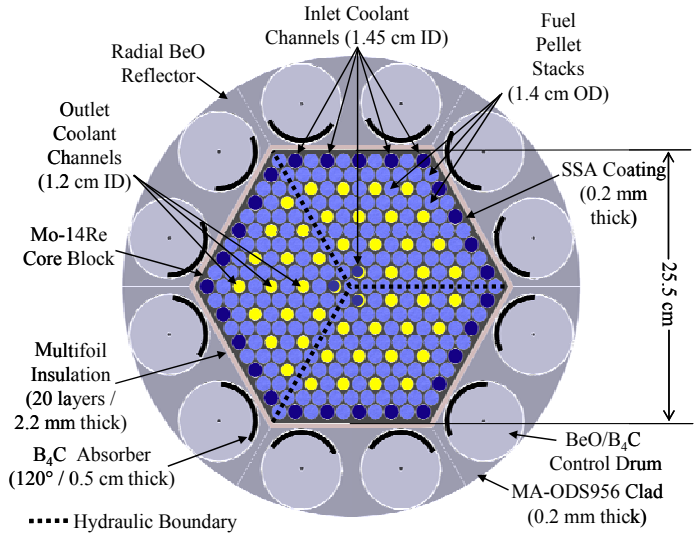

Fig. 30 Radial cross-sectional view of S^4 reactor.

mass of the radiator water heat pipes, the geometric aspect ratio of the vapor space, $H_V/(2R_V) = 0.5$ (Tournier and El-Genk, 2006).

The water heat pipes have a 0.2 mm thick titanium (Ti) wick made of 3 layers of 150-mesh screen and that has an average pore radius of 50 μm and a volume porosity of 0.70 (Table 8). To decrease the liquid pressure losses in the wick and hence, raise the capillary limit, the wick is separated from the Ti liner by a ~ 0.1 mm-thick liquid annulus (Fig. 31b, and Table 8). The diameter of the water heat pipes varies from 1.73 to 2.54 cm, and the armor thickness is 1.58 mm to 1.85 mm. These armor thicknesses are sufficient to withstand the nominal pressure of the water vapor in the heat pipes (< 2.5 MPa). Heat pipes with integral C-C fins have been successfully manufactured using a T-300 fiber, an angle interlocking weave architecture, and pitch densification (Rovang *et al.*, 1991; Juhasz and Rovang, 1995). Burst tests showed that a C-C shell with a diameter of 2.54 cm and a thickness of only 0.864 mm (C-C bulk density is 1650 kg/m^3) could withstand an internal pressure greater than 4.1 MPa. The lightweight (1800 kg/m^3) C-C armor and integrated fins used in the present radiator water heat pipes significantly reduce its specific mass (kg/m^2), without compromising the structural strength. The NaK ducts in the radiator panels are protected with 2.0 to 4.0 mm-thick C-C armor (Fig. 31a),

Table 8 Design parameters and materials of the radiator water heat pipes in the S^4 reactor power system.

Parameter	Value
Vapor flow area per heat pipe (mm^2)	150 – 400
Porous wick material / type	Ti / 150-mesh
Wick average porosity	0.70
Wick effective pore radius (μm)	50.0
Wick thickness (mm) / number of layers	0.20 / 3
Wall material / thickness (mm)	Ti / 0.10
C-C fin and armor density (kg / m^3)	1,800.
C-C fin thickness (mm)	0.5
C-C emissivity	0.90
Space sink temperature (K)	200

allowing the outward and inward facing surfaces of the ducts to radiate into space.

6.2 Performance of Radiator Water Heat Pipes

A design optimization model of the segmented radiator panels was coupled to a model that calculates the operation limits and parameters of the water heat pipes (El-Genk and Tournier, 2004a and 2004b; Tournier and El-Genk, 2005). These include the liquid and vapor pressures and temperatures and the temperature drops in the structures of the evaporator and condenser sections, including the C-C wall and titanium liner, the water annulus, and the water saturated titanium wick. Due to the low power throughput for radiator water heat pipes, the heat flux in the evaporator section is very low (< 6.5 W/cm^2) and capillary is the only limit of concern. Also, the vapor temperature along the pipes is almost constant and equal to that of saturation at the average condenser temperature.

The small pore size in the wick of the water heat pipes (Table 8) increases the capillary pressure head developing in the evaporator section. The liquid annulus between the titanium liner and the porous wick (> 65 μm thick) reduces the water flow pressure losses, though they increase the radial temperature drops in the evaporator and condenser sections. The vapor pressure losses in the heat pipes are negligible. The radiator water heat pipes (Fig. 31) operate nominally at or below 50% of their capillary limits. Thus, if one (or more) fails, adjacent heat pipes would easily carry the power rejection load.

The design optimization of the water heat pipes radiator panels are for fixed NaK inlet and exit temperatures of 530 and 395 K (Fig. 29) and circulation pressure losses of 10 kPa. For the nominal heat rejection load of each radiator panel (54 kW_{th}), the NaK mass flow rate in each secondary loop is 0.8976 kg/s (Fig. 29). In the forward segments of the radiator panels, the hottest water heat pipe at the entrance of the NaK duct is the longest and carries the largest power throughput of 320 W (Fig. 32). It has vapor and water flow areas of 4.0 cm^2 and 12 mm^2 (annulus thickness of 152 μm), 2.54 cm ID, and 1.85 mm thick C-C armor. It nominally operates at ~ 46% of the capillary limit (Fig. 33) and vapor temperature and pressure of 485 K and 1.97 MPa.

By contrast, the shortest water heat pipes in the forward segment of the radiator panels operate much cooler (427 K and 0.52 MPa), and each transport a much lower power of 45 W each (Fig. 32). They operate at 30% of the capillary limit (Fig. 33) and have smaller vapor and liquid flow areas of 1.5 cm^2 and 3 mm^2 (annulus thickness of 68 μm), an ID = 1.73 cm, and 1.58 mm thick C-C armor. The hottest, and shortest heat pipes in the rear deployable segments of the radiator panels have a vapor and water flow area of 2 cm^2 6.1 mm^2 (annulus thickness of ~111 μm), and a diameter of 1.97 cm, and nominally reject 154 W each (Fig. 32).

The ducts of the liquid NaK in the rear radiator segments are 2.88 mm high and 8 cm wide at the minor diameter and 16 cm wide at the major diameter. Because the shortest heat pipes at the entrance of the NaK ducts in these segments are the hottest (491 K vapor temperature), each carries 154 W, and operates at the highest vapor pressure of 2.24 MPa. All heat pipes in the radiator rear segments have the same C-C armor thickness (1.82 mm), dictated by the longest heat pipes for meteoroids protection. The longest heat pipes operate cooler (427 K) at a much lower vapor pressure (0.52 MPa). Each transports more power (200 W) than the shortest heat pipes, because their condenser section is much longer. They have vapor and liquid flow areas of 4 cm^2 and 9.2 mm^2 (annulus width of 118 μm), and 2.54 cm OD.

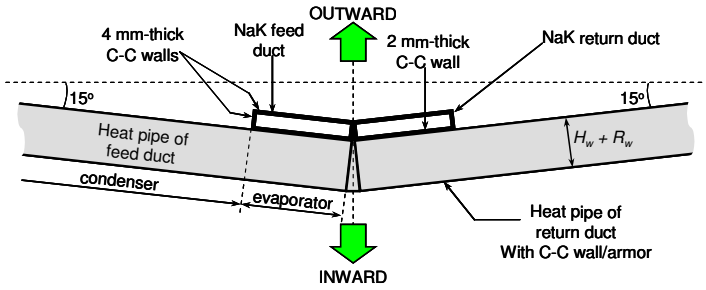

(a) Longitudinal View (Not to Scale)

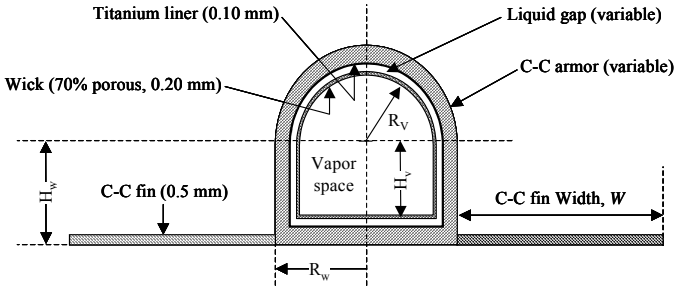

(b) Cross-Sectional View

Fig. 31 Radiator water heat pipe with C-C armor and fins.

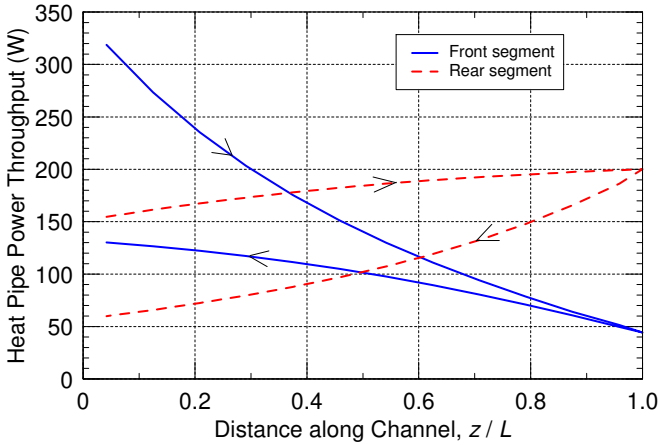

Fig. 32 Power throughput estimates for radiator water heat pipes.

The liquid NaK feed and return ducts of the forward segments of the radiator panels are 2.85 mm high, and 16 cm wide at the major diameter and 4 cm wide at the minor diameter. Along the liquid NaK flow ducts in these segments, the power throughput decreases rapidly from 320 W to 45 W as the length of the water heat pipes decreases from 1.13 m to 0.268 m (Fig. 32). The water flow pressure losses in these heat pipes decrease from 650 Pa to a minimum of 500 Pa, then increase to 590 Pa. These heat pipes operate at 46.3% to a minimum of 28% of their capillary limits, and at 30% at the rear end of the forward radiator segments (Fig. 33).

The temperature drops are highest in the evaporator and condenser structures of the water heat pipes followed, a distant second, by those in the NaK flow and duct wall (Fig. 34). In Figure 34, subtracting the temperature drops in the NaK flow and duct wall from the total gives the sum of the temperature drops in the evaporator and condenser

Global Digital Central
ISSN: 2155-658X

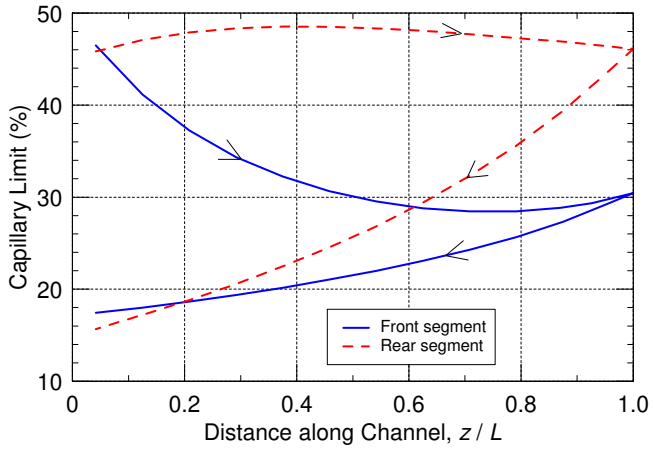

Fig. 33 Capillary limit of water heat pipes in front and rear radiator panel segments.

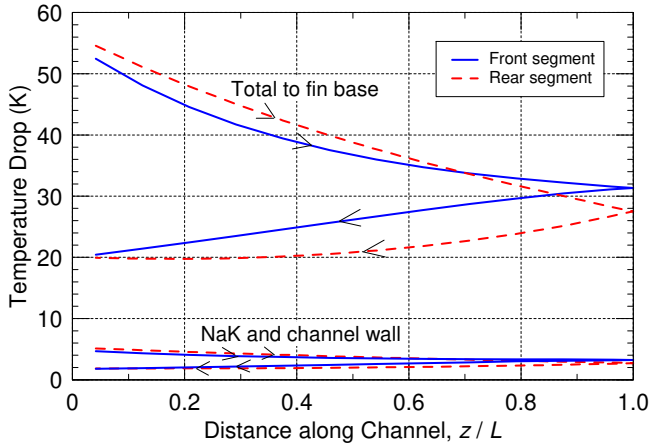

Fig. 34 Temperature drops in radiator water heat pipes.

structures of the water heat pipes. The temperature drop between the condenser wall and the base of the C-C fin varies from 8 K to 20 K.

7. SUMMARY AND CONCLUSIONS

Alkali metal heat pipes are considered for uses in space nuclear reactor power systems to reliably and redundantly transport the heat generated in reactor to the energy conversion subsystem, and to develop light-weight and redundant heat rejection radiators. Water heat pipes are also considered for uses in radiators of power systems that employ either CBC or FPSE, because of the low heat rejection temperature (< 550 K). Space reactors that operate at 900 – 1400 K could be cooled using liquid-metal heat pipes with either Na (900 –1100 K) or Li (1100 – 1400 K) working fluids. The heat rejection temperatures dictate the working fluid of the radiator heat pipes; potassium for 600 – 800 K, rubidium for 500 – 700 K, and water for $\leq$ 500 K. These working fluids would be frozen at startup in orbit or at destination.

In addition to a review of the operation and design constraints pertinent to the uses of water and alkali-metal heat pipes in space nuclear reactor power systems, this paper presented and demonstrated the capabilities of modeling the transient operation of these heat pipes, including the startup from a frozen state. In addition to presenting models validation with reported experimental results for Na and Li heat pipes, results of design optimization of alkali metal and water heat pipes for uses in a number of space reactor power systems are presented and discussed. The results are for heat rejection radiator panels with C-C armored and finned K, Rb, Cs and water heat pipes, and for Na heat pipes for reactor cooling in the SAIRS space power system. Results show that these heat pipes could be designed with ample margins from their prevailing operation limits.

Experiments and modeling results confirmed that the startup of alkali metal heat pipes from a frozen state is practically possible and safe, though the input power should be kept sufficiently low until the working fluid is fully thawed and the vapor flow along the heat pipe transitions to the continuum regime. The very low vapor pressures of alkali metals prolong the startup time of the heat pipes to many hours. However, this time could be shortened by adding a small amount of noble gases and increasing the length of the condenser section to accommodate these gases during steady-state operation.

The startup of water heat pipes from a frozen state comes with different challenges; primarily among them are the low thermal conductivity, high latent heat of melting and the increase in density upon thawing. The latter could partially uncover the wick in the evaporator section before the heat pipes are fully thawed. On the other hand, the startup time of water heat pipes from a frozen state is relatively shorter than for alkali-metal heat pipes because water vapor start in the continuum flow regime. Nonetheless, a reliable and safe startup of water heat pipes from a frozen state would require using a very low input power until the ice in the wick along the heat pipes is fully thawed, and the water return flow in the wick is established.

ACKNOWLEDGMENTS

This work is sponsored by the Institute for Space and Nuclear Power Studies at the University of New Mexico (UNM-ISNPS).

NOMENCLATURE

A	cross-section flow area or surface area (m^2)
A_w	Wick cross-sectional area (m^2)
D_{vapor}	Diameter of vapor space in heat pipe (m)
F	Radiation view factor
h_{fg}	Latent heat of vaporization (J / kg)
H_V	Straight height of D-shaped vapor space (m)
K	Permeability of porous wick (m^2)
L	Length (m)
$\bar{L}$	Effective length (m), $\bar{L} = L_a + (L_{ev} + L_{cd})/2$
$\dot{m}$	Coolant mass flow rate (kg / s)
M_L	Figure of merit (W/m^2), $M_L = \sigma h_{fg} / \nu_L$
Q	Thermal power (W)
R_c	Radius of curvature of L-V interface (m)
R_p	Average pore radius of wick (m)
R_V	Radius of D-shaped vapor space (m)
R_W	Radius of D-shaped, armored heat pipe (m)
t	Time (s)
T	Temperature (K)
T_{tr}	Vapor flow transition temperature (K)
W	Width of C-C fin in radiator segment (m)
z	Axial coordinate along heat pipe (m)

Greek Symbols

α	Aspect ratio of D-shaped heat pipe, $\alpha = H_V / D_V$
ΔP	Pressure drop or rise (Pa)
η	Efficiency
θ_c	Contact angle (radiant), $\cos\theta_c = R_p / R_c$
μ	Coolant dynamic viscosity (kg/m.s)
ν_L	Kinematic viscosity of liquid (m^2/s)
ρ	Density (kg / m^3)
σ	Liquid surface tension (N / m)

Subscripts and Superscripts

a	Adiabatic section
cap	Capillary pressure head or limit
cd	Heat pipe condenser
ev	Heat pipe evaporator
fus	Fusion (melting) point

Global Digital Central
ISSN: 2155-658X

L Liquid phase
V Vapor phase

REFERENCES

Anderson, W. G. (2005), "Evaluation of Heat Pipes in the Temperature Range of 450 to 700 K," *Proc. Space Technology and Applications International Forum (STAIF-2005)*, M. S. El-Genk, Ed., American Institute of Physics, AIP-CP-746, **1**, pp. 171 – 178.

Angelo, J. A., Jr. and Buden, D. (1985), *Space Nuclear Power*, Orbit Book Co., Inc., Malabar, FL.

Barrett, M. J. and Johnson, P. K. (2005), "Performance and Mass Modeling Subtleties in Closed-Brayton-Cycle Space Power Systems," *Proc. 3rd Int. Energy Conversion Engineering Conference (IECEC-2005)*, American Institute of Aeronautics and Astronautics, Paper No. AIAA-2005-5700.

Barrett, M. J. and Reid, B. M. (2004), "System Mass Variation and Entropy Generation in 100-kWe Closed-Brayton-Cycle Space Power Systems," *Proc. Space Technology and Applications International Forum (STAIF-2004)*, M. S. El-Genk, Ed., American Institute of Physics, AIP-CP-699, **1**, pp. 445 – 452.

Begg, L. L., Wuchte, T. J. and Otting, W. D. (1992), "STAR-C Thermionic Space Nuclear Power System," *Proc. 9th Symposium on Space Nuclear Power Systems*, M. S. El-Genk and M. D. Hoover, Eds., American Institute of Physics, CONF-920104, AIP-CP-246, **1**, pp. 114 – 119.

Bevard, B. B. and Yoder, G. L. (2003), "Technology Development Program for an Advanced Potassium Rankine Power Conversion System Compatible with Several Space Reactor Designs," *Proc. Space Technology and Applications International Forum (STAIF-2003)*, M. S. El-Genk, Ed., American Institute of Physics, AIP-CP-654, **1**, pp. 629 – 634.

Buckman, R. W. (2004), "Nuclear Space Power Systems Materials Requirements," *Proc. Space Technology and Applications International Forum (STAIF-2004)*, M. S. El-Genk, Ed., American Institute of Physics, AIP-CP-699, **1**, pp. 815 – 820.

Busse, C. A. (1967), "Pressure Drop in the Vapor Phase of Long Heat Pipes," *Proc. Thermionic Conversion Specialist Conference*, Institute of Electrical and Electronics Engineers, pp. 391 – 398.

Caillat, T., Borshchevsky, A., Snyder, J. and Fleurial, J.-P. (2000), "High Efficiency Segmented Thermoelectric Unicouples," *Proc. Space Technology and Applications International Forum (STAIF-2000)*, M. S. El-Genk, Ed., American Institute of Physics, AIP-CP-504, **3**, pp. 1508 – 1512.

Determan, W. R. and Hagelston, G. (1992), "Thermionic In-Core Heat Pipe Design and Performance," *Proc. 9th Symposium on Space Nuclear Power Systems*, M. S. El-Genk and M. D. Hoover, Eds., American Institute of Physics, CONF-920104, AIP-CP-246, **3**, pp. 1046 – 1051.

Deverall, J. E., Kemme, J. E. and Florschuetz, L. W. (1970), *Sonic Limitations and Startup Problems of Heat Pipes*, Los Alamos Scientific Laboratory Report No. LA-4518 (accession No. N71-18944), Los Alamos, NM.

DiStefano, J. R. (1989), "Review of Alkali Metal and Refractory Alloy Compatibility for Rankine Cycle Applications," in *Space Nuclear Power Systems 1988*, M. S. El-Genk and M. D. Hoover, Eds., Orbit Book Co., 1989, **9**, pp. 299 – 310.

El-Genk, M. S. (1994), *A Critical Review of Space Nuclear Power and Propulsion 1984 - 1993*, AIP Press, New York, NY.

El-Genk, M. S. (2008a), "Space Reactor Power Systems with No Single Point Failures," *J. Nuclear Engineering and Design*, **238**, 2245 – 2255. doi:10.1016/j.nucengdes.2008.02.026

El-Genk, M. S. (2008b), "Space Nuclear Reactor Power System Concepts with Static and Dynamic Energy Conversion," *Energy Conversion and Management*, **49** (3), 402 – 411. doi:10.1016/j.enconman.2007.10.014

El-Genk, M. S., Buksa, J. J. and Seo, J. T. (1988), "Decay Heat Thermal Management of an SP-100 System," in *Space Nuclear Power Systems 1987*, M. S. El-Genk and M. D. Hoover, Eds., Orbit Book Company, Inc., 1988, **6**, pp. 99 – 110.

El-Genk, M. S., Huang, L. and Tournier, J.-M. (1995), "Transient Experiments of an Inclined Copper-Water Heat Pipe," *J. Thermophysics and Heat Transfer*, **9** (1), pp. 109 – 116. doi:10.2514/3.635

El-Genk, M. S. and Paramonov, D. V. (1999), "Thermionic Conversion," *Encyclopedia of Electrical and Electronics Engineering*, J. G. Webster, Ed., John Wiley and Sons, Inc., **22**, pp. 49 – 67.

El-Genk, M. S. and Saber, H. H. (2003), "High Efficiency Segmented Thermoelectric Unicouple for Operation between 973 K and 300 K," *Energy Conversion and Management*, **44**, 1069 – 1088. doi:10.1016/S0196-8904(02)00109-7

El-Genk, M. S. and Saber, H. H. (2005), "Performance Analysis of Cascaded Thermoelectric Converters for Advanced Radioisotope Power Systems," *Energy Conversion and Management*, **46**, 1083 – 1105. doi:10.1016/j.enconman.2004.06.019

El-Genk, M. S., Saber, H. H., Caillat, T. and Sakamoto, J. (2006), "Test Results and Performance Comparisons of Coated and UN-Coated Skutterudite-Based Segmented Unicouples," *Energy Conversion and Management*, **47**, 174 – 200. doi:10.1016/j.enconman.2005.03.023

El-Genk, M. S. and Tournier, J.-M. (1995), "A Critical Review of Free-Molecular and Transition Flow Regimes in Heat Pipes," *Proc. 9th International Heat Pipe Conference*, M. A. Merrigan, Ed., LANL Technical Report LA-UR-97-1500, **1**, pp. 497 – 508.

El-Genk, M. S. and Tournier, J.-M. (2002a), "Performance Comparison of Potassium and Sodium Vapor Anode, Multi-Tube AMTEC Converters," *Energy Conversion and Management*, **43**, 1931 – 1951. doi:10.1016/S0196-8904(01)00142-X

El-Genk, M. S. and Tournier, J.-M. (2002b), "Challenges and Fundamentals of Modeling Heat Pipes' Startup from a Frozen State," *Proc. Space Technology and Applications International Forum (STAIF-2002)*, M. S. El-Genk, Ed., American Institute of Physics, AIP-CP-608, **1**, pp. 127 – 138.

El-Genk, M. S. and Tournier, J.-M. (2004a), "SAIRS – Scalable AMTEC Integrated Reactor Space Power System," *Progress in Nuclear Energy*, **45** (1), 25 – 69. doi:10.1016/j.pnucene.2004.08.002

El-Genk, M. S. and Tournier, J.-M. (2004b), "Performance Analysis of Potassium Heat Pipes Radiator for HP-STMCs Space Reactor Power System," *Proc. Space Technology and Applications International*

Forum (STAIF-2004), M. S. El-Genk, Ed., American Institute of Physics, AIP-CP-699, **1**, pp. 793 – 805.

El-Genk, M. S. and Tournier, J.-M. (2005), "A Review of Refractory Metal Alloys and Mechanically Alloyed-Oxide Dispersion Strenghtened Steels for Space Nuclear Power Systems," *J. Nuclear Materials*, **340**, 93 – 112.
doi:10.1016/j.jnucmat.2004.10.118

El-Genk, M. S. and Tournier, J.-M. (2006a), "High Temperature Water Heat Pipes Radiator for a Brayton Space Reactor Power System," *Proc. Space Technology and Applications International Forum (STAIF-2006)*, M. S. El-Genk, Ed., American Institute of Physics, AIP-CP-813, **1**, pp. 716 – 729.

El-Genk, M. S. and Tournier, J.-M. (2006b), "DynMo-TE: Dynamic Simulation Model of Space Reactor Power System with Thermoelectric Converters," *J. Nuclear Engineering and Design*, **236**, 2501 – 2529.
doi:10.1016/j.nucengdes.2006.03.004

El-Genk, M. S., Tournier, J.-M. and Gallo, B. M. (2010), "Dynamic Simulation of a Space Reactor System with Closed Brayton Cycle Loops," *J. Propulsion and Power*, **26** (3), 394 – 406.
doi:10.2514/1.46262

Faghri, A. (1995), *Heat Pipe Science and Technology*, Taylor Francis.

Faghri, A., Buchko, M. and Cao, Y. (1991), "A Study of High Temperature Heat Pipes with Multiple Heat Sources and Sinks, Part I: Experimental Methodology and Frozen Startup Profiles," *J. Heat Transfer*, **113** (4), 1003 – 1009.
doi:10.1115/1.2911193

Gallo, B. M. and El-Genk, M. S. (2009), "Brayton Rotating Units for Space Reactor Power Systems," *Energy Conversion and Management*, **50** (9), 2210 – 2232.
doi:10.1016/j.enconman.2009.04.035

Glass, D. E., Merrigan, M. A., Sena, J. T. and Camarda, C. J. (1999), "Startup and Transient Performance of a Nb-1%Zr Potassium Heat Pipe," *J. Thermophysics and Heat Transfer*, **13** (1), 153 – 155.
doi:10.2514/2.6414

Gunther, N. G. (1990), *Characteristics of the Soviet TOPAZ II Space Power System*, Report No. SPI-52-1, Space Power Inc., San Jose, CA.

Harty, R. and Mason, L. (1993), "100-kWe Lunar/Mars Surface Power Utilizing the SP-100 Reactor with Dynamic Conversion," *Proc. 10th Symposium on Space Nuclear Power and Propulsion*, M. S. El-Genk and M. D. Hoover, Eds., American Institute of Physics, AIP-CP-271, **2**, pp. 1065 – 1071.

Houts, M. G., Poston, D. I. and Emrich, W. J., Jr. (1998), "Heatpipe Power System and Heatpipe Bimodal system Development Status," *Proc. Space Technology and Applications International Forum (STAIF-1998)*, M. S. El-Genk, Ed., American Institute of Physics, AIP-CP-420, **3**, pp. 1189 – 1195.

Huang, L. and El-Genk, M. S. (1993), "Transient Performance of an Inclined Water Heat Pipe with a Screen Wick," *National Heat Transfer Conference, Heat Pipes and Capillary Pumped Loops*, A. Faghri et al., Eds., HTD-Vol. **236**, pp. 87 – 92.

Ivanovskii, M. N., Sorokin, V. P. and Yagodkin, I. V. (1982), *The Physical Principles of Heat Pipes*, translated by R. Berman and G. Rice, Oxford University Press, New York, NY, Section 2.2 pp. 34 – 56, and pp. 73 – 140.

Josloff, A. T., Shepard, N. F., Chan, T. S., Greenwood, F. C., Deane, N. A., Stephen, J. D. and Murata, R. E. (1994), "SP-100 Generic Flight System Design and Early Flight Options," *Proc. 11th Symposium on Space Nuclear Power Systems*, M. S. El-Genk and M. D. Hoover, Eds., American Institute of Physics, CONF-940101, AIP-CP-301, **2**, pp. 533 – 538.

Juhasz, A. J. and Rovang, R. D. (1995), "Development of Lightweight Prototype Carbon-Carbon Heat Pipe with Integral Fins and Metal Foil Liner," *Proc. 12th Symposium on Space Nuclear Power Systems*, M. S. El-Genk and M. D. Hoover, Eds., American Institute of Physics, CONF-950110, AIP-CP-324, **1**, pp. 135 – 143.

King, J. C. and El-Genk, M. S. (2001), "Review of Refractory Materials for Alkali Metal Thermal-to-Electric Conversion Cells," *J. Propulsion and Power*, **17** (3), 547 – 555.
doi:10.2514/2.5810

King, J. C. and El-Genk, M. S. (2004), "A Methodology for the Neutronics Design of Space Nuclear Reactors," *Proc. Space Technology and Applications International Forum (STAIF-2004)*, M. S. El-Genk, Ed., American Institute of Physics, AIP-CP-699, **1**, pp. 319 – 329.

Loeb, L. B. (1934), *The Kinetic Theory of Gases*, McGraw-Hill Book Co., New York, NY, pp. 290 – 300.

Marriott, A. T. and Fujita T. (1994), "Evolution of SP-100 System Designs," *Proc. 11th Symposium on Space Nuclear Power and Propulsion*, M. S. El-Genk and M. D. Hoover, Eds., American Institute of Physics, CONF-940101, **1**, pp. 157 – 169.

Merrigan, M. A. (1985), "Heat Pipe Technology Issues," in *Space Nuclear Power Systems 1984*, M. S. El-Genk and M. D. Hoover, Eds., Orbit Book Company, 1985, **2**, pp. 419 – 426.

Merrigan, M. A. and Trujillo, V. L. (1992), "Moderated Heat Pipe Thermionic Reactor (MOHTR) Module Development and Test," *Proc. 9th Symposium on Space Nuclear Power Systems*, M. S. El-Genk and M. D. Hoover, Eds., American Institute of Physics, CONF-920104, **3**, pp. 1038 – 1045.

Mills, J. C., Determan, W. R. and Van Hagan, T. H. (1994), "S-PRIME/TI-SNPS Conceptual Design Summary," *Proc. 11th Symposium on Space Nuclear Power Systems*, M. S. El-Genk and M. D. Hoover, Eds., American Institute of Physics, CONF-940101, **2**, pp. 695 – 700.

Moriarty, M. P. and Determan, W. R. (1989), "SP-100 Advanced Radiator Designs for Thermoelectric and Stirling Applications," *Proc. 24th Intersociety Energy Conversion Engineering Conference*, IEEE, Paper No. 899618, **2**, pp. 1245 – 1250.

Ozisik, N. M. (1980), *Heat Conduction*, Wiley-Interscience, New York, NY, Chapter 10, pp. 406 – 412.

Paramonov, D. V. and El-Genk, M. S. (1997), "Test Results of Ya-21u Thermionic Space Power System," *J. Nuclear Technology*, **117** (1), 1 – 14.

Ponnappan, R., Boehman, L. I. and Mahefkey, E. T. (1990), "Diffusion-Controlled Startup of a Gas-Loaded Liquid-Metal Heat Pipe," *J. Thermophysics and Heat Transfer*, **4** (3), 332 – 340.
doi:10.2514/3.185

Poston, D. I., Kapernick, R. J. and Guffee, R. M. (2002), "Design and Analysis of the SAFE-400 Space Fission Reactor," *Proc. Space*

Technology and Applications International Forum (STAIF-2002), M. S. El-Genk, Ed., American Institute of Physics, AIP-CP-608, **1**, pp. 578 – 588.

Prenger, F. C., Jr. (1979), *Heat Pipe Computer Program (HTPIPE) User's Manual,* Report No. LA-8101-M, Los Alamos National Laboratory, Los Alamos, NM, November 1979.

Ranken, W. A. (1982), *Status of high-Temperature Heat Pipe Technology*, Report No. LA-UR-82-3340, Los Alamos National Laboratory, Los Alamos, NM, 1982.

Ranken, W. A. (1990), "Historical View of Thermionic Reactor Development," *Proc. 7th Symposium on Space Nuclear Power Systems*, M. S. El-Genk and M. D. Hoover, Eds., Institute for Space Nuclear Power Studies, CONF-900109, **1**, pp. 393 – 399.

Rathjen, K. A. and Jiji, L. M. (1971), "Heat Conduction with Melting or Freezing in a Corner," *J. Heat Transfer*, **93**, 101 – 109. doi:10.1115/1.3449740

Reay, D. (2006), *Heat Pipes, Theory, design and Applications*, Butterwork-Heinemannn, 5th Edition.

Reid, R. S., Merrigan, M. A. and Sena, J. T. (1991), "Review of Liquid Metal Heat Pipe Work at Los Alamos," *Proc. 8th Symposium on Space Nuclear Power Systems*, M. S. El-Genk and M. D. Hoover, Eds., American Institute of Physics, CONF-910116, **3**, pp. 999 – 1008.

Reid, R. S., Sena, J. T. and Martinez, A. L. (1999), *Heat Pipe Development for Advanced Energy Transport Concepts, Phase II – Progress Report Covering the Period October 1, 1997, to September 30, 1998*, Report No. LA-13549-PR, Los Alamos National Laboratory, Los Alamos, NM, February 1999.

Ring, P. J., Sayre, E. D. and Sena, J. T. (2003), "SAFE-100 Module Fabrication and Test," *Proc. Space Technology and Applications International Forum (STAIF-2003)*, M. S. El-Genk, Ed., American Institute of Physics, AIP-CP-654, **1**, pp. 96 – 100.

Rosenfeld, J. H., Ernst, D. M., Lindemuth, J. E., Sanzi, J. L., Geng, S. M. And Zuo, J. (2004), "An Overview of Long Duration Sodium Heat Pipe Tests," *Proc. Space Technology and Applications International Forum (STAIF-2004)*, M. S. El-Genk, Ed., American Institute of Physics, AIP-CP-699, **1**, pp. 140 – 147.

Rovang, R. D., Hunt, M. E., Dirling, R. B., Jr. and Holzl, R. A. (1991), "SP-100 High-Temperature Advanced Radiator Development," *Proc. 8th Symposium on Space Nuclear Power Systems*, M. S. El-Genk and M. D. Hoover, Eds., American Institute of Physics, CONF-910116, **2**, pp. 702 – 707.

Ryan, M. A., Shields, V. B., Cortez, R. H., Lara, L., Homer, M. L. and Williams, R. M. (2000), "Lifetime of AMTEC Electrodes: Molybdenum, Rhodium-Tungsten, and Titanium Nitride," *Proc. Space Technology and Applications International Forum (STAIF-2000)*, M. S. El-Genk, Ed., American Institute of Physics, AIP-CP-504, **2**, pp. 1377 – 1382.

Scheidegger, A. E. (1974), *The Physics of Flow through Porous Media*, 3rd Edition, University of Toronto Press.

Schmitz, P. C., Tower, L., Dawson, R., Blue, B. and Dunn, P. (1994), "Preliminary SP-100/Stirling Heat Exchanger Designs," *Proc. 11th Symposium on Space Nuclear Power Systems*, M. S. El-Genk and M. D. Hoover, Eds., American Institute of Physics, CONF-940101, AIP-CP-301, **1**, pp. 447 – 455.

Schmitz, P. C., Schreiber, J. G. and Penswick, B. (2005), "Feasibility Study of a Nuclear-Stirling Power Plant for the Jupiter Icy Moons Orbiter," *Proc. Space Technology and Applications International Forum (STAIF-2005)*, M. S. El-Genk, Ed., American Institute of Physics, AIP-CP-746, **1**, pp. 738 – 749.

Schreiber, J. (2001), "Power Characteristics of a Stirling Radioisotope Power System over the Life of the Mission," *Proc. Space Technology and Applications International Forum (STAIF-2001)*, M. S. El-Genk, Ed., American Institute of Physics, AIP-CP-552, **2**, pp. 1011 – 1016.

Shepard, N. F., Biddiscombe, R., Chan, T. S., Deane, N. A., Fallas, T., Kirpich, A. S., Murata, R. E., Salamah, S. and Stephen, J. D. (1994), "20-kWe Space Reactor Power System using Brayton Cycle Conversion," *Proc. 11th Symposium on Space Nuclear Power Systems*, M. S. El-Genk and M. D. Hoover, Eds., American Institute of Physics, AIP-CP-301, **1**, pp. 427 – 439.

Thieme, L., Schreiber, J. and Mason, L. (2002), "Stirling Technology Development at NASA GRC," *Proc. Space Technology and Applications International Forum (STAIF-2002)*, M. S. El-Genk, Ed., American Institute of Physics, AIP-CP-608, **2**, pp. 872 – 879.

Thieme, L. and Schreiber, J. (2004), "Advanced Technology Development for Stirling Converters," *Proc. Space Technology and Applications International Forum (STAIF-04)*, M. S. El-Genk, Ed., American Institute of Physics, AIP-CP-699, **1**, pp. 432 – 439.

Tournier, J.-M. and El-Genk, M. S. (1995), "Transient Analysis of the Startup of a Water Heat Pipe from a Frozen State," *J. Numerical Heat Transfer, Part B, Applications*, **28**, 461 – 486. doi:10.1080/10407789508913756

Tournier, J.-M. and El-Genk, M. S. (1996), "A Vapor Flow Model for Analysis of Liquid-Metal Heat Pipes Startup from a Frozen State," *Int. J. Heat and Mass Transfer*, **39** (18), 3767 – 3780. doi:10.1016/0017-9310(96)00066-X

Tournier, J.-M. and El-Genk, M. S. (2002), "Current Capabilities of HPTAM for Modeling High-Temperature Heat Pipes Startup from a Frozen State," *Proc. Space Technology and Applications International Forum (STAIF-2002)*, M. S. El-Genk, Ed., American Institute of Physics, AIP-CP-608, **1**, pp. 139 – 147.

Tournier, J.-M. and El-Genk, M. S. (2003), "Startup of a Horizontal Lithium-Molybdenum Heat Pipe from a Frozen State," *Int. J. Heat and Mass Transfer*, **46**, 671 – 685. doi:10.1016/S0017-9310(02)00324-1

Tournier, J.-M. and El-Genk, M. S. (2004), "Reactor Lithium Heat Pipes for HP-STMCs Space Reactor Power System," *Proc. Space Technology and Applications International Forum (STAIF-2004)*, M. S. El-Genk, Ed., American Institute of Physics, AIP-CP-699, **1**, pp. 781 – 792.

Tournier, J.-M. and El-Genk, M. S. (2005), "Liquid Metal Heat Pipes Radiator for Space Nuclear Reactor Power Systems," *Proc. 3rd International Energy Conversion Engineering Conference (IECEC-2005)*, held 15-18 August, 2005 in San Francisco, CA, American Institute of Aeronautics and Astronautics, Paper No. AIAA 2005-5701.

Tournier, J.-M. and El-Genk, M. S. (2006), "Liquid Metal Loop and Heat Pipes Radiator for Space Reactor Power Systems," *J. Propulsion and Power*, **22** (5), 1117 – 1134. doi:10.2514/1.20031

Trujillo, V. L., Keddy, E. S. and Merrigan, M. A. (1990), "High-Temperature, Deployable, Membrane Heat Pipe Radiator Element: Demonstration and Status," *Proc. 7th Symposium on Space Nuclear Power Systems*, M. S. El-Genk and M. D. Hoover, Eds., Institute for Space and Nuclear Power Studies, CONF-900109, **2**, pp. 870 – 874.

Wolff, F. and Viskanta, R. (1988), "Solidification of a Pure Metal at a Vertical Wall in the Presence of Liquid Superheat," *International J. Heat and Mass Transfer*, **31** (8), 1735 – 1744.
doi:10.1016/0017-9310(88)90285-2

Woloshun, K. A., Merrigan, M. A. and Best, E. D. (1989), "HTPIPE – A Steady-State Heat Pipe Analysis Program," in *Space Nuclear Power Systems 1988*, M. S. El-Genk and M. D. Hoover, Eds., Orbit Book Company, 1989, **9**, pp. 395 – 403.

Yoder, G. L. and Graves, R. L. (1985), "Analysis of Alkali Liquid Metal Rankine Space Power Systems," in *Space Nuclear Power Systems 1984*, M. S. El-Genk and M. Hoover, Eds., Orbit Book Company, 1985, **4**, pp 231 – 237.

Zinkle, S. J., Ott, L. J., Ingersoll, D. T., Ellis, R. J. and Grossbeck, M. L. (2002), "Overview of Materials Technologies for Space Nuclear Power and Propulsion," *Proc. Space Technology and Applications International Forum (STAIF-2002)*, M. S. El-Genk, Ed., American Institute of Physics, AIP-CP-608, **1**, pp. 1063 – 1074.